SANDIA REPORT

SAND98–2046
Unlimited Release
Printed January 1999

Laboratory Characterization of Mechanical and Permeability Properties of Dynamically Compacted Crushed Salt

K. D. Mellegard, T. W. Pfeifle, and F. D. Hansen

Prepared by
Sandia National Laboratories
Albuquerque, New Mexico 87185 and Livermore, California 94550

Sandia is a multiprogram laboratory operated by Sandia Corporation, a Lockheed Martin Company, for the United States Department of Energy under Contract DE-AC04-94AL85000.

Sandia National Laboratories

Issued by Sandia National Laboratories, operated for the United States Department of Energy by Sandia Corporation.

Available to DOE and DOE contractors from
Office of Scientific and Technical Information
P.O. Box 62
Oak Ridge, TN 37831

Prices available from (615) 576-8401, FTS 626-8401

Available to the public from
National Technical Information Service
U.S. Department of Commerce
5285 Port Royal Rd
Springfield, VA 22161

NTIS price codes
Printed copy: A05
Microfiche copy: A01

DISCLAIMER

Portions of this document may be illegible in electronic image products. Images are produced from the best available original document.

SAND98-2046
Unlimited Release
Printed January 1999

Laboratory Characterization of Mechanical and Permeability Properties of Dynamically Compacted Crushed Salt

K.D. Mellegard, T.W. Pfeifle
RE/SPEC Inc.
Rapid City, SD 57709-0725

F.D. Hansen
Sandia National Laboratories
P. O. Box 5800
Albuquerque, NM 87185-1395

ABSTRACT

The U.S. Department of Energy (DOE) plans to dispose of transuranic wastes at the Waste Isolation Pilot Plant (WIPP), a geologic repository located at a depth of about 655 meters. The WIPP underground facility is located in the bedded salt of the Salado Formation. Access to the facility is provided through vertical shafts, which will be sealed after decommissioning to limit the release of hazardous waste from the repository and to limit flow into the facility.

Because limited data are available to characterize the properties of dynamically compacted crushed salt, Sandia National Laboratories authorized RE/SPEC to perform additional tests on specimens of dynamically compacted crushed salt. These included shear consolidation creep, permeability, and constant strain-rate triaxial compression tests. A limited number of samples obtained from the large compacted mass produced by Hansen and Ahrens (1996) were available for use in the testing program. Thus, additional tests were performed on samples that were prepared on a smaller scale device in the RE/SPEC laboratory using a dynamic-compaction procedure based on the full-scale construction technique.

The laboratory results were expected to (1) illuminate the phenomenology of crushed-salt deformation behavior and (2) add test results to a small preexisting database for purposes of estimating parameters in a crushed-salt constitutive model. The candidate constitutive model for dynamically compacted crushed salt was refined in parallel with this laboratory testing.

This page intentionally left blank

TABLE OF CONTENTS

FIGURES

TABLES

This page intentionally left blank

1.0 INTRODUCTION

1.1 Background

The U.S. Department of Energy (DOE) plans to dispose of transuranic wastes at the Waste Isolation Pilot Plant (WIPP) located in southeastern New Mexico. The WIPP is designed to be a full-scale geologic repository, and its underground facility is located in the bedded salt of the Salado Formation at a depth of about 655 meters below ground surface. Access to the facility is provided through vertical shafts. Because these shafts comprise direct communication between lithologic units and connect the underground facility to the surface, they will be sealed to limit the release of hazardous waste from the repository and to limit flow into the facility.

One of the primary seal components in the Salado Formation is dynamically compacted crushed salt. Crushed salt has been selected because of its chemical compatibility with the host salt rock. In addition, crushed salt is an attractive sealing material because its permeability is expected to decrease as the surrounding host salt rock creeps into the shaft and reduces the volume of sealing material (crushed salt). The initial fractional density of the crushed salt at placement will be 0.9 (Sandia National Laboratories, 1996), where fractional density is defined as the ratio of the current bulk density to the density of intact salt (i.e., 2.16 g/cc (Callahan et al., 1998)). Hansen and Ahrens (1998) demonstrated that initial fractional densities of 0.9 could be achieved in a full-scale construction technology demonstration. Their study produced large blocks from which laboratory-scale specimens were subcored for use in laboratory programs.

Because limited data are available to characterize the properties of dynamically compacted crushed salt; the Sandia National Laboratories (SNL) Repository Isolation Systems Department authorized RE/SPEC to perform additional tests on specimens of dynamically compacted crushed salt. The types of tests to be performed included shear consolidation creep, permeability, and constant strain-rate triaxial compression. A limited number of samples obtained from the large compacted mass produced by Hansen and Ahrens were available for use in the testing program. Thus, additional tests were performed on samples that were prepared on a smaller scale device in the RE/SPEC laboratory using a dynamic-compaction procedure based on the full-scale construction technique.

The purpose of the laboratory work was twofold. The laboratory results were expected to (1) illuminate the phenomenology of crushed-salt deformation behavior and (2) add test results to a small preexisting database for purposes of estimating parameters in a crushed-salt constitutive model. The candidate constitutive model for dynamically compacted crushed salt (Callahan et al., 1998b) was refined in parallel with this laboratory testing and the current model refinements have been published (Callahan et al., 1998a). The work was conducted under RE/SPEC's QA Program

as specified in the document, "Quality Assurance Project Plan: Rock Mechanics Analysis Support for Sandia National Laboratories, AG-4911 (RSI Job 325), RSI QAPP-09.

1.2 Organization

In addition to this introduction, this report is organized into five additional chapters and two appendices. Chapter 2.0 provides a description of the specimens used for the testing and the equipment and procedures used to fabricate the laboratory-scale specimens. Chapter 3.0 describes the test equipment and procedures that were used in the study and is followed by Chapter 4.0, which summarizes the results of the testing. Concluding remarks are in Chapter 5.0 followed by a list of cited references in Chapter 6.0. The two appendices contain technical memoranda that outline specific work conducted on crushed salt.

2.0 SPECIMENS

There were two sources of dynamically compacted crushed-salt specimens. The first was the large-scale, dynamically compacted crushed salt recovered from the dynamic-compaction demonstration study (Hansen and Ahrens, 1998) that produced a compacted mass greater than 40 m^3. The second source of specimens was provided by the laboratory-scale, dynamic-compaction device designed and built at RE/SPEC.

The specimens derived from the large-scale dynamically compacted mass provided by SNL (Hansen and Ahrens, 1998) were prepared by dry-coring them from the large blocks and then finishing the ends to produce cylindrical specimens suitable for testing. Finished specimens had a diameter of 100 millimeters and lengths up to 200 millimeters. Some specimens had lengths less than 200 millimeters because of dimensional limitations imposed by the irregular geometry of the large blocks. Hansen and Ahrens also produced a small amount of dynamically compacted material from initial intermediate technology demonstration trials. A few specimens from the intermediate-scale trials were used for early permeability work by Brodsky (Appendix B).

Some of the dynamically compacted crushed-salt specimens used for this laboratory program were fabricated in a laboratory-scale compaction device. This device approximated the compaction technique envisioned for the shaft sealing design. The laboratory-scale compaction device is shown in Figure 2-1. The system uses a 30-pound cylindrical hammer that can be dropped from a height of 1.52 meters (5 feet) through a rail guide that directs the position where the hammer strikes the crushed salt that is contained in a cylindrical mold. The hammer diameter is 50.8 millimeters (2 inches) which equals the radius of the mold. The hammer guide was constructed such that it could be rotated to strike along any desired radius of the specimen. This feature was included in the design to mimic the compaction technique used in the large-scale compaction device operated by SNL. The mold was fabricated from two standard Proctor split compaction molds. The assembled mold is capable of producing a cylindrical sample with a diameter of 101.6 millimeters (4 inches) that can be machined into a specimen with a nominal length of 200 millimeters.

Brodsky (1994) has characterized the disaggregated crushed salt that was used as the raw material for making the laboratory-scale specimens. The crushed salt was subjected to a sieve analysis, and all particles larger than 9.5 millimeters were crushed to pass a 9.5-millimeter sieve and then added back into the mixture. The particle size limit of 9.5 millimeters was selected to ensure the largest particle was less than a tenth of the specimen diameter, which was about 100 millimeters. The sieve analysis of the material satisfying the 9.5-millimeter limit indicated a particle size of approximately 1.8 millimeters at the 50^{th} percentile.

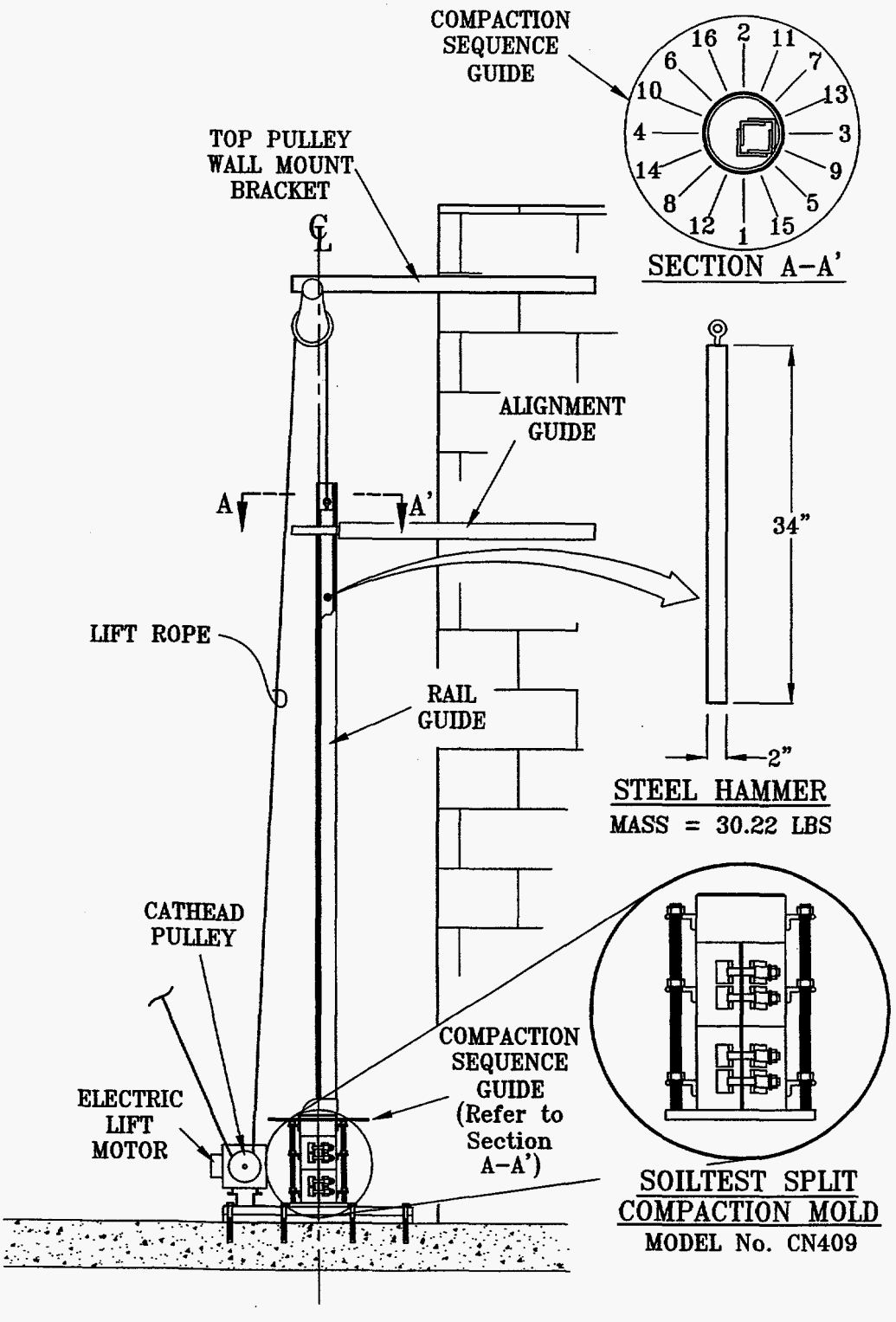

Figure 2-1. Laboratory-scale dynamic-compaction device.

During shakedown testing of the compaction device, the question arose regarding how much friction loss was imparted to the hammer by the rail guide. A simple, comparative method was used to assess the frictional effect by first dropping the hammer from varying heights onto a lead ball target *without* the rail guide in place (free fall) and then repeating the drops *with* the rail guide in place (guided fall). The results of that testing are presented in Figure 2-2, which plots the final deformed thickness of the lead ball versus the drop height. There is one curve for the free-fall tests and one curve for the guided-fall tests. The deformed thickness of the lead balls were compared to determine what the equivalent free-fall drop height was for a given guided-fall drop height. That comparison gave an equivalent free-fall height for each guided-fall height, and the relationship is shown in Figure 2-3. For a guided-fall drop height of 1.52 meters (5 feet), the equivalent free-fall drop height was approximately 1.34 meters (4.4 feet). The equivalent free-fall drop height is the value that was used to calculate the three times, modified-Proctor energy level that was imparted to the specimen during the compaction process.

The specimens fabricated with the laboratory-scale device were identified as RS/DCCS/n, where n took on values of 1, 2, 3, etc. to designate individual specimens. After machining the end of the compacted cylindrical sample, the specimens had final nominal dimensions of 100-millimeter diameter and 200-millimeter length. The starting material was wetted with a WIPP brine that had previously been manufactured at RE/SPEC using distilled water and the same crushed salt used to fabricate the specimens, so the specimen moisture content was nominally 1.6 percent by weight. The initial dry fractional density of the specimens was about 0.9 (assuming intact salt has a density of 2.16 g/cc).

The moisture content of the laboratory-scale specimens was determined using standard laboratory procedures, as described below. Samples of the disaggregated crushed salt were placed in metal containers of known mass. Each sample and container was weighed using a balance having a resolution of 0.01 gram and placed in an oven regulated to a temperature of 110°C. Periodically, the samples and containers were removed from the oven and weighed to monitor the loss of water during drying. When the mass of each sample/container changed by less than 0.01 gram over a 24-hour period, it was assumed that all of the moisture in the sample had been removed. The mass of water contained in the specimen was calculated as the difference between the initial and final masses of the sample/container. Using the data from the drying procedure, values were calculated for moisture content of the samples and density of the test specimens using the following expressions:

$$w = 100\frac{M_w}{M_{ds}} \qquad (2\text{-}1)$$

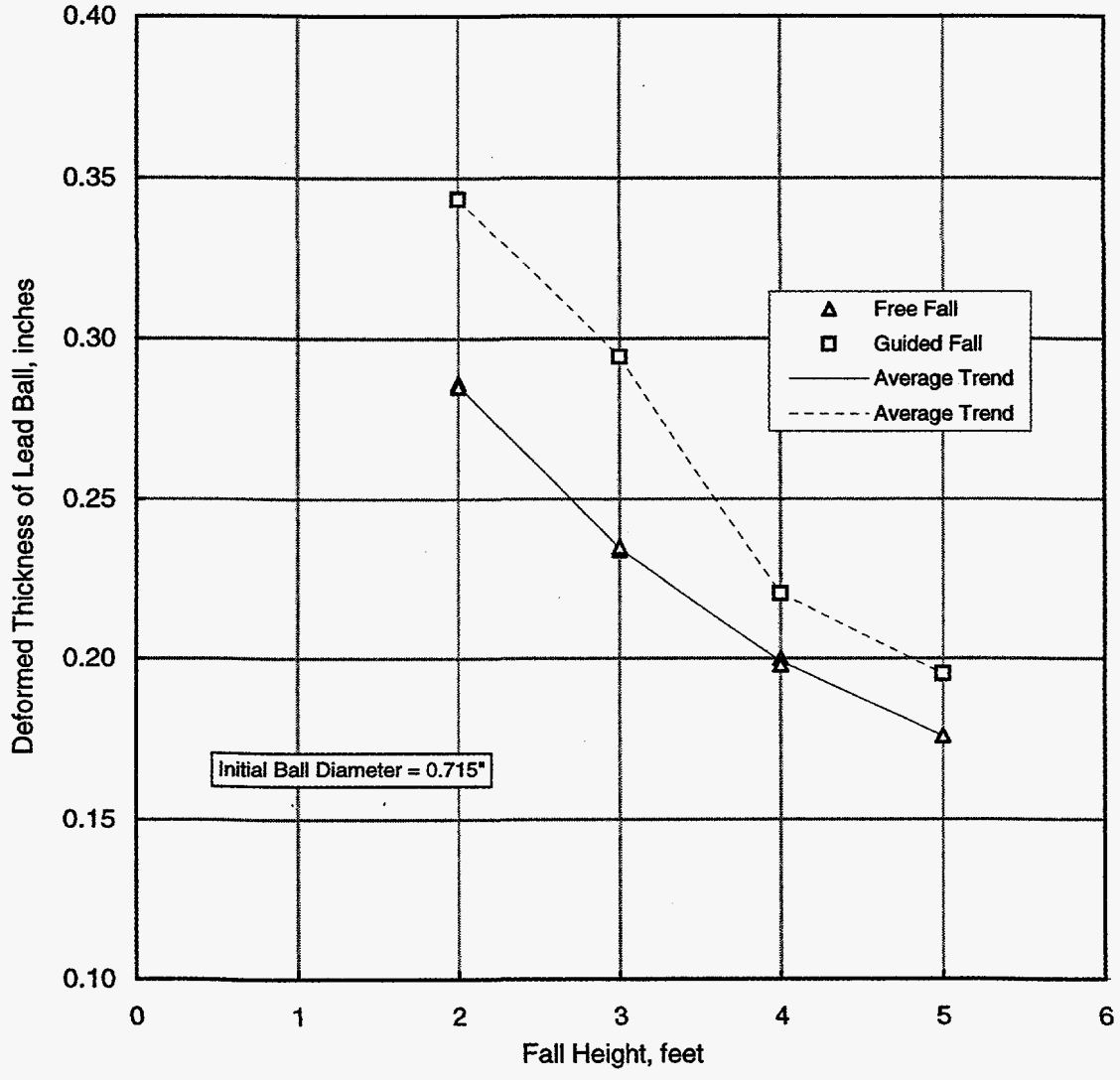

Figure 2-2. Lead ball deformation as a function of drop height.

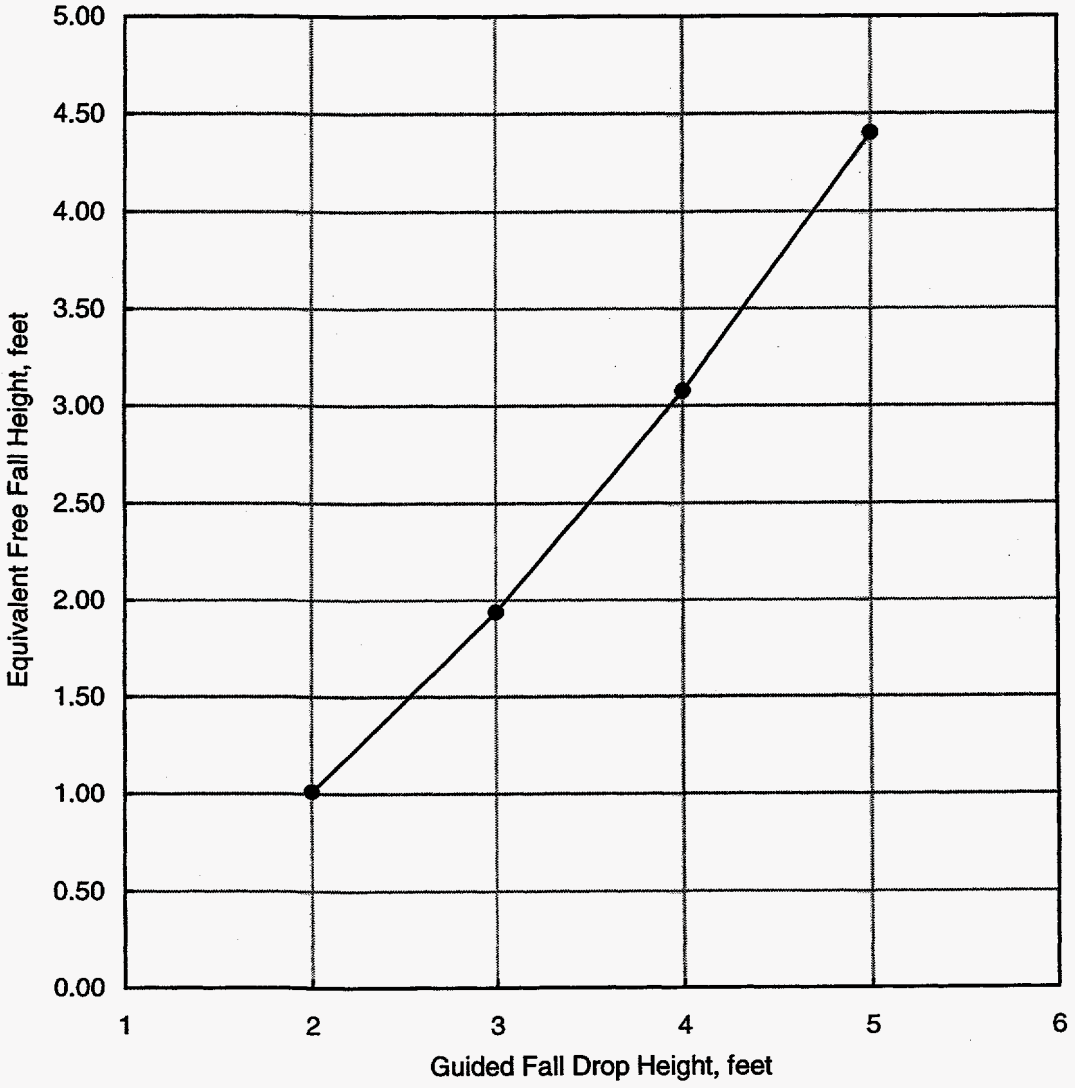

Figure 2-3. Equivalent free-fall drop height as a function of guided-fall drop height.

$$\rho = \frac{M_{ws}}{V_s\left(1+\frac{w}{100}\right)} \tag{2-2}$$

where:

w = percent moisture content
ρ = dry density
M_{ds} = mass of the dry sample
M_{ws} = mass of the wet sample
M_w = mass of water contained in the sample
V_s = volume of specimen.

Volume was determined for finished specimens having regular solid geometries (e.g., solid cylinders) using direct measurements of the specimen dimensions (i.e., length and diameter).

A summary of the moisture contents and densities of the laboratory-scale specimens fabricated at RE/SPEC and used in this study is presented in Table 2-1. The first column is the specimen identification label, and the second column indicates the type of testing applied to that specimen. The third column gives the moisture content for each specimen, and the fourth column lists the dry fractional density for each specimen before it was tested. These dry fractional densities were calculated assuming the density of intact salt is 2.16 g/cc.

A summary of the moisture contents and densities of the large-scale specimens made available by the Hansen and Ahrens experiment and used in this study is presented in Table 2-2. This table is similar to the previous table presented for laboratory-scale specimens produced by RE/SPEC. The fractional densities were calculated assuming the density of intact salt is 2.16 g/cc.

Table 2-1. Laboratory-Scale, Dynamically Compacted Crushed-Salt Specimen

Specimen Identification	Test Type	Moisture Content (%)	Initial Dry Fractional Density
RS/DCCS/1	Shear Consolidation	1.66	0.904
RS/DCCS/3	Shear Consolidation	1.63	0.905
RS/DCCS/4	Shear Consolidation	1.59	0.904
RS/DCCS/5	Shear Consolidation	1.55	0.898
RS/DCCS/6	Constant Strain Rate	1.47	0.901
RS/DCCS/10	Shear Consolidation	1.49	0.907
RS/DCCS/11	Constant Strain Rate	1.68	0.912
RS/DCCS/15	Shear Consolidation	1.77	0.901
RS/DCCS/21	Constant Strain Rate	1.62	0.907

Table 2-2. Large-Scale, Dynamically Compacted Crushed-Salt Specimens

Specimen Identification	Test Type	Moisture Content (%)	Initial Dry Fractional Density
DCCS/3/3/3-1	Brine Permeability	Saturated	0.889
CS/DC2/T2S-1/1[(a)]	Brine Permeability	Saturated	0.863
CS/DC1/8-3[(a)]	Brine Permeability	Saturated	0.864
DCCS/3/2/3-1	Shear Consolidation	1.53	0.889
DCCS/3/1/2-1	Shear Consolidation	1.52	0.889
DCCS/3/3/3-1	Gas Permeability	0.44	0.889
DCCS/3/2/1-1	Gas Permeability	0.44	0.901
DCCS/3/1/1-4	Gas Permeability	0.44	0.889
DCCS/3/3/1-4	Gas Permeability	0.44	0.901
DCCS/3/2/2-1	Gas Permeability	1.27	0.899

(a) These specimens were initially tested using a gas permeant (Appendix B).

3.0 TEST EQUIPMENT AND PROCEDURES

The laboratory program encompassed three different types of experiments: shear consolidation creep, constant strain-rate triaxial compression, and permeability. Petrographic studies of test specimens are contained in this chapter, following test descriptions. The equipment and procedures are discussed in the separate sections.

3.1 Shear Consolidation

The shear consolidation tests were effectively standard creep tests. The specimens were initially loaded hydrostatically to the level of specified confining pressure (radial stress). Following the hydrostatic loading, the axial stress was increased by 4 MPa while the confining pressure was held constant. Each of the tests was the same in this regard, in that each was subjected to a 4 MPa axial stress difference. Only the specified level of the confining pressure varied among tests. Following the application of the axial stress difference, the axial stress difference was held constant at 4 MPa while data were acquired during the creep consolidation phase. At the termination of the test, an unload/reload cycle was performed by reducing the applied axial force to drop the stress difference to near zero and then reapplying the axial force to reload the specimen to a stress difference of 4 MPa before totally unloading the specimen. The ascending loading data from the reloading portion of the cycle were used for estimating elastic constants. The following sections present additional details on the equipment and procedures used for the shear consolidation testing.

3.1.1 Load Frame

Figure 3-1 presents a cross section of a typical consolidation frame with prominent components labeled for reference. The frames used single-ended, triaxial pressure vessels. A linear actuator (hydraulic cylinder) bolted to the base of the load frame advanced the loading piston, which in turn, applied axial compressive force to the specimen. Confining pressure was applied to the jacketed specimens by pressurizing the sealed vessel chamber with silicone oil. A dilatometer system maintained constant confining pressure and provided the volumetric measurement. The testing machines could apply compressive axial loads up to 1.5 MN and confining pressures up to 70 MPa. The heating system, including seals on the pressure vessel, could maintain specimen temperatures up to 200°C, although all the current testing was performed at 25°C. A control panel located near the load frames housed accumulators, hydraulic pumps, pressure intensifiers, transducer signal conditioners, temperature controllers, and confining pressure controllers for two adjacent test frames.

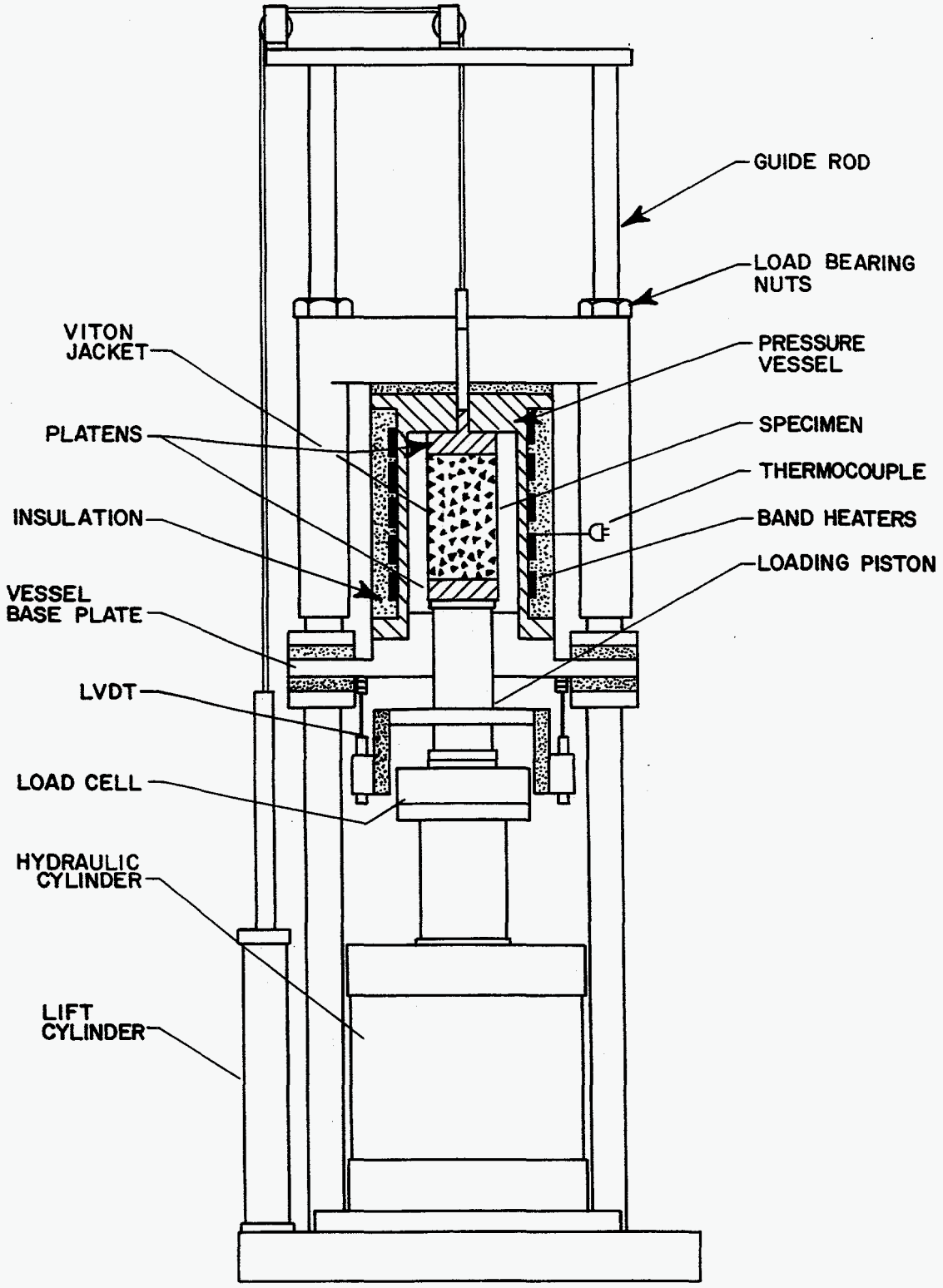

Figure 3-1. Schematic of static triaxial test system.

3.1.2 Instrumentation

Axial force was measured by a load cell located in the load train outside the pressure vessel, while confining pressure was measured by a pressure transducer located in the line between the intensifier and the pressure vessel. Temperature was measured by a thermocouple embedded in the wall of the pressure vessel. The relationship between the actual specimen temperature and the thermocouple measurement has been determined by calibration at several temperatures spanning the operating range. Two linear variable differential transformers (LVDTs) mounted outside the pressure vessel monitored displacement of the loading piston relative to the bottom of the pressure vessel. Volumetric deformation was measured using a dilatometer. With this technique, volumetric deformation was determined at fixed pressure by first measuring the volume of oil that the dilatometer supplied to the pressure vessel, and then compensating for the axial deformation measured by the LVDTs. A stroke transducer was mounted on the dilatometer shaft to provide a signal proportional to the volume of oil, either supplied to or extracted from the pressure vessel.

The transducers used to collect force, pressure, deformation, and temperature data were calibrated under documented RE/SPEC procedures using standards traceable to the National Institute of Standards and Technology (NIST). Each transducer was calibrated in its normal operating position on the test system so that the signal conditioners, filters, and analog-to-digital converters were included within the end-to-end calibration. Calibration constants were determined for each transducer from a linear, least-squares regression of indicated reading versus standard input. Readings were collected at 20 standard inputs equally spaced over the range of the transducer. These constants were verified immediately before testing began by comparing the predicted response of the transducer using these constants, with the standard input applied in ten equally spaced steps over the calibrated range. Acceptance criteria developed for the verification process were based on the following accuracy criteria: 1 percent of reading for force and pressure transducers, 2 percent of reading for deformation transducers, and ±1°C for thermocouples. The accuracy specifications included both linearity and repeatability.

3.1.3 Control

Test system variables were controlled by a personal computer running data acquisition and control software programmed for loading and maintaining creep tests. Temperature was maintained by a software routine that regulated power to the band heaters on the vessel based on a feedback signal provided by a thermocouple in the pressure vessel wall. Confining pressure was controlled by inputting the pressure transducer signal to another routine that maintained the confining pressure within a 20 kPa deadband around the desired pressure. Through the use of digital I/O signals, the pressure control software instructed the dilatometer to advance or retreat,

depending upon whether the lower or upper edge of the deadband had been reached. Axial load was adjusted by a similar software routine to maintain a constant axial stress on the specimen. The program determined the current cross-sectional area of the specimen from the outputs of the deformation transducers and then adjusted the load to maintain constant stress. The deadband on load under this control was 0.4 kN. A standby diesel generator provided electrical power to the test systems during periods of commercial electrical power outages.

3.2 Constant Strain Rate

Three constant strain-rate tests were performed on the laboratory-scale, dynamically compacted crushed salt. All three tests were performed at the same confining pressure (1 MPa), but three different axial strain rates were imposed (0.5×10^{-7}, 1.0×10^{-7}, and 2.0×10^{-7} s^{-1}). The following sections present additional information on the equipment and procedure used to perform the constant strain-rate testing.

3.2.1 Load Frame

A computerized, servohydraulic test frame manufactured by MTS Systems was used to perform the constant strain-rate tests. The test frame is equipped with two reaction posts that provide a total axial force capacity of 0.5 MN. A custom pressure vessel designed by RE/SPEC was mounted in the test frame to provide triaxial compression capability.

The load frame configuration is shown in Figure 3-2 where prominent components have been labeled for reference. The pressure vessel is designed for confining pressure of up to 70 MPa and is fitted with resistance heaters and insulation blankets allowing operation at temperatures of 200°C. However, for this work, the confining pressure was limited to 1 MPa and the tests were all performed at a temperature of 20°C.

3.2.2 Instrumentation

The test system instrumentation was typical of most triaxial compression experiments. The load cell attached to the test frame crosshead recorded total axial force and confining pressure was measured by a pressure transducer located in the line leading from a hydraulic intensifier to the vessel. For specimen deformation measurements, the specimen was encased in a protective jacket and instrumented with deformation transducers, as shown in Figure 3-3. The extensometers shown in Figure 3-3 directly recorded the axial and radial deformations of the specimen over their respective gage lengths. The axial extensometer was an MTS Model 632.90C unit with deformation sensors in both arms. The sensor outputs are combined and scaled into a single analog output voltage, which gets measured by an analog-to-digital converter

(ADC). Simultaneous ADC measurements are made of the output signal provided by the radial deformation extensometer. The radial deformation extensometer is a strain-gaged ring (i.e., lateral disk gage) rigidly connected to two vertical mounting posts that contact the specimen at opposite ends of a diameter located at specimen midheight.

All data were logged with respect to time by using the clock provided by the Digital Equipment Corporation (DEC) 11/73 microprocessor which was the platform running the data acquisition and control software program. The software was written in MTS MultiUser BASIC which is the programming language provided with the system by MTS Systems. The acquired data were archived onto the computer disk and then transferred over a local area network to make them available for postprocessing using standard spreadsheets; e.g., EXCEL 97.

The original specimen dimensions were those measured on the bench before the specimen was encased in its protective jacket. The current specimen dimensions were determined from the deformation measurements made during the test. The change in diameter was measured directly by the lateral disk gage (LDG) mounted across a diameter at the midheight of the specimen. The change in specimen length was calculated by assuming the axial strain measured over the axial extensometer gage length represented the average strain in the specimen. The area of the loading ram was always larger than the area of the specimen.

3.2.3 Control

There were two segments of the load path used to perform a constant strain-rate test. The first segment imposed a hydrostatic load path up to the level of the desired confining pressure, which, for these tests, was 1 MPa. This segment was performed in load control with the servohydraulic control system advancing the axial force and the confining pressure to effect a hydrostatic pressurization rate of 0.02 MPa/second. At this slow pressurization rate, the extensometers were not subjected to thermal drift that could be caused by adiabatic heating of the confining fluid (Mellegard et al., 1993). At the end of the hydrostatic pressurization ramp, the stresses were held constant and the consolidation rates were monitored. If the axial strain rate during hydrostatic consolidation was larger than the axial strain rate specified for the next segment of loading, the load path was held at the hydrostatic state until the consolidation rate fell below the specified axial strain rate. The reason for this delay follows from the constraints imposed by the test machine loading system. If the consolidation rate were higher than the axial strain rate specified for the constant strain-rate segment, the control system would sense a feedback signal that is too high and would attempt to reduce the axial strain rate by removing axial load. Since a test is initiated at a hydrostatic state, the removal of axial load would cause the axial stress to fall below the hydrostatic stress state and a state of triaxial extension would be imposed. The test system

RSI-100-88-002

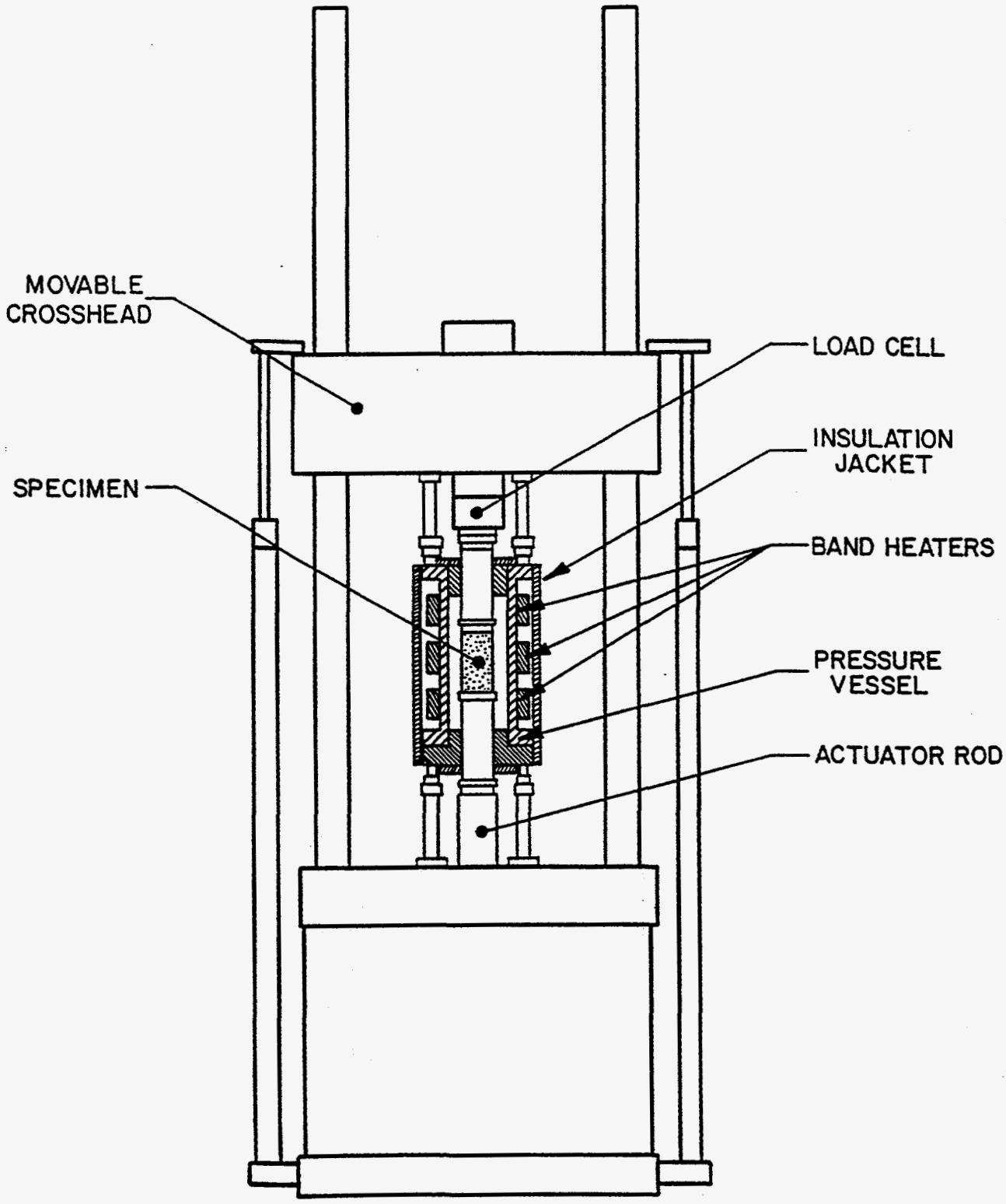

Figure 3-2. Schematic of dynamic triaxial test system.

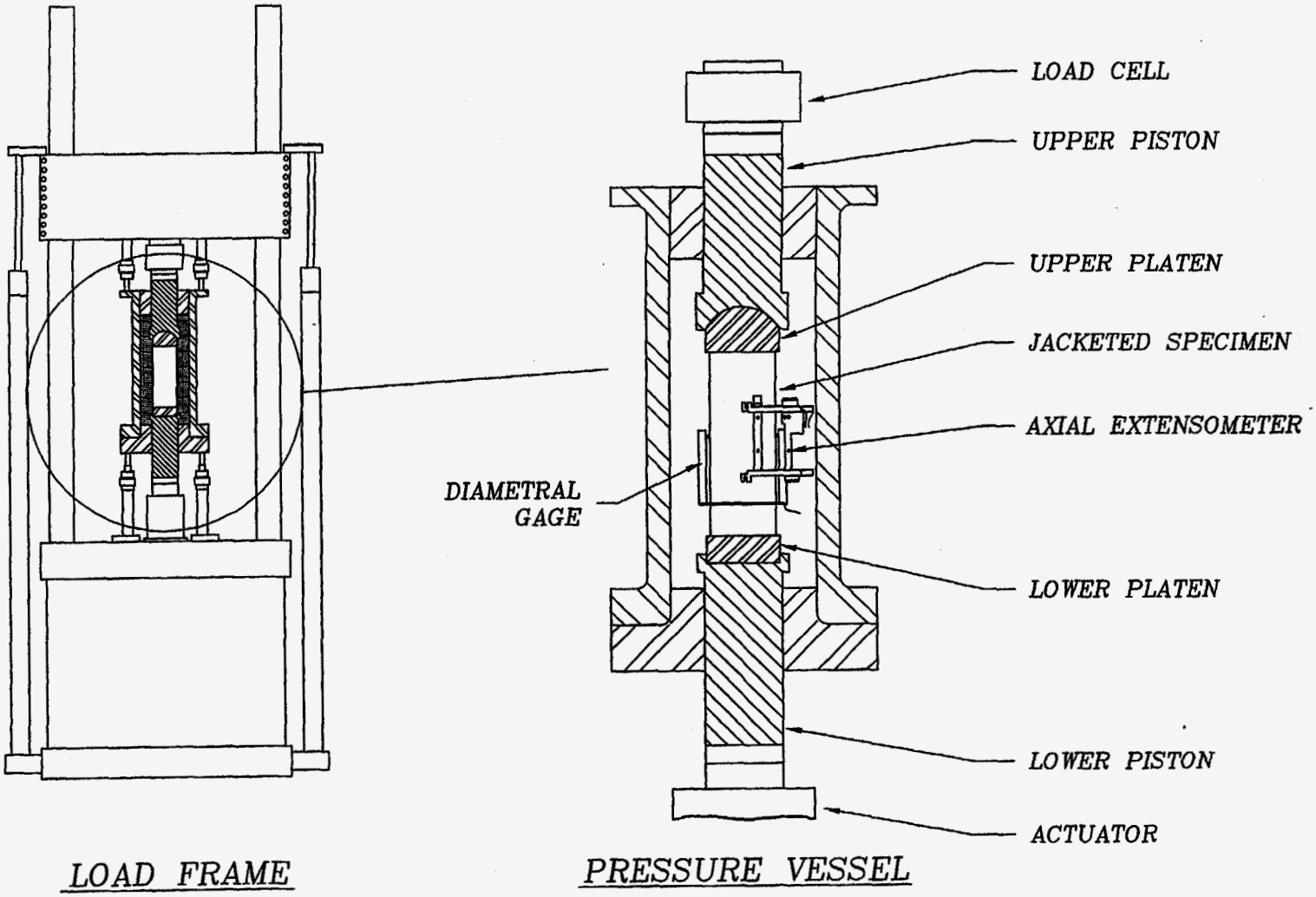

Figure 3-3. Constant strain-rate test setup.

used here will not support triaxial extension because the vessel is a single-ended apparatus. Thus, if the system attempted to impose triaxial extension, the axial loading column would simply decouple and all of the axial load would be removed, effectively terminating the test immediately.

After waiting for the consolidation rates to decrease to an appropriate level, the constant strain-rate segment of the test started. Upon entering the constant strain-rate segment, the mode of axial force control was switched from load to axial strain; i.e., the feedback signal for controlling application of axial load was switched from the load cell to the axial extensometer mounted on the specimen. The command signal provided by the computer was ramped linearly to cause the axial extensometer to deform at the specified constant axial strain rate while the confining pressure was held constant. The axial load increased as required, depending upon the specimen response. The loading was terminated when the deformation transducers reached their maximum operating range.

3.3 Permeability

Specimens identified for permeability testing were placed inside protective flexible Viton sleeves or jackets which were secured to two metal platens positioned at either end of the specimen, as shown in Figure 3-4. The jacket served to protect the specimen from the hydraulic fluid (silicone oil) used to apply radial stress during permeability measurements. Each platen was equipped with a 3.2-millimeter-diameter vent drilled along the central axis of the platen to provide access to porous felt metal disks placed in the specimen/platen interfaces. These disks were used to ensure one-dimensional flow parallel to the central axis of the specimen by inducing uniform permeant pressure across the specimen ends. The specimen assembly shown in Figure 3-4 was placed inside the pressure vessel of the testing frame depicted schematically in Figure 3-1, which is the same test system that was used for the shear consolidation tests.

For those specimens tested with a brine permeant, the specimen exit was connected to the buret measurement system shown in Figure 3-5. Brine permeant was supplied to the specimen inlet by a pressurized accumulator. The charge pressure to the accumulator was controlled manually with a valve located on a nitrogen gas bottle and measured by a pressure transducer located in the hydraulic line at the inlet to the specimen. A hydrostatic stress of 1 MPa was applied to the external surfaces of the specimen by pressurizing the annulus between the specimen and the pressure vessel wall. The valve located at the specimen inlet was then opened to permit the flow of brine through the test specimen. The flow rate at the specimen exit and brine pressure at the specimen inlet were then recorded by reading the buret level and the pressure transducer, respectively. The pressure at the inlet was limited to 0.34 MPa (about one-third the confining pressure) to ensure that the flow paths were through the specimen and not

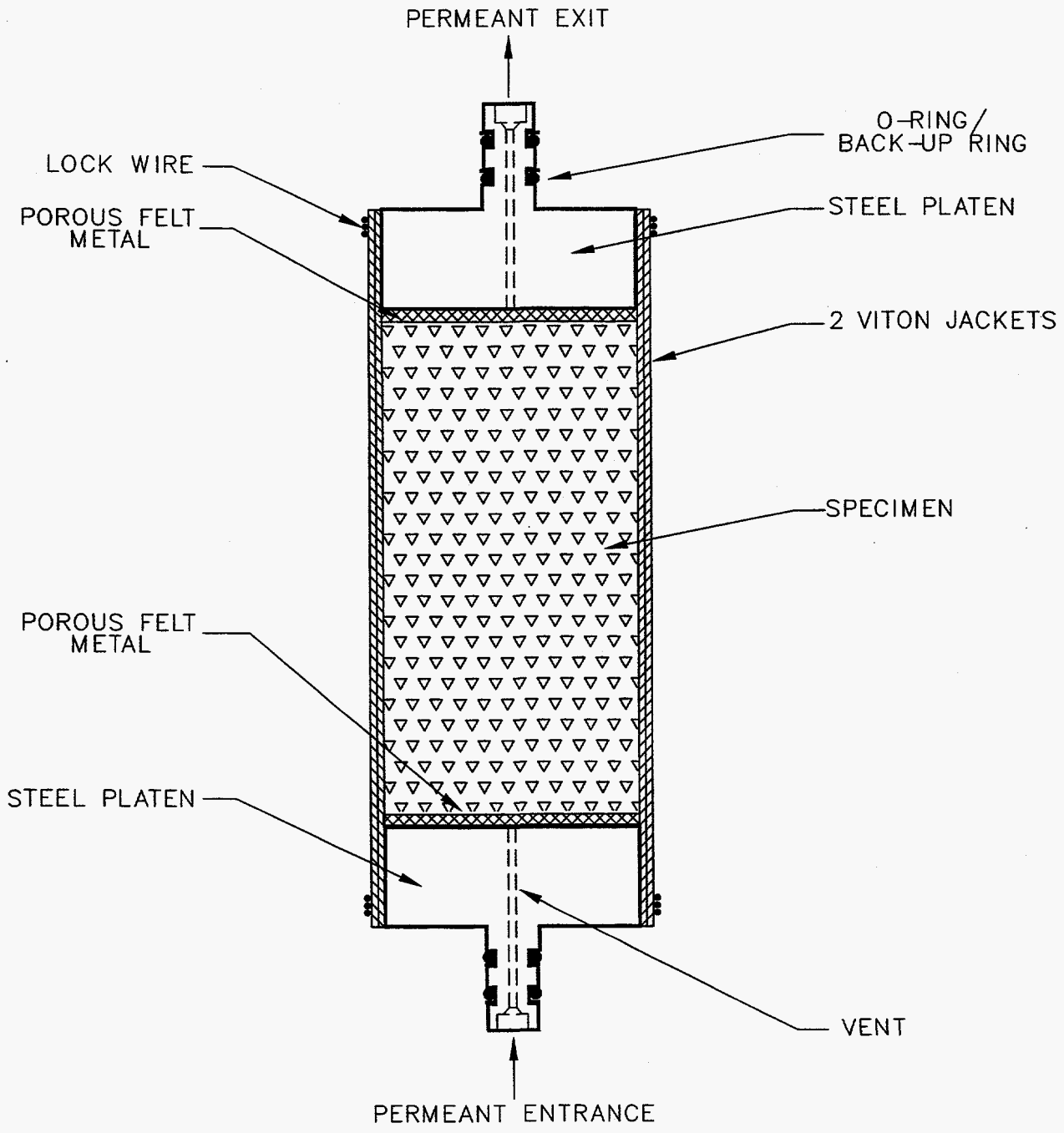

Figure 3-4. Jacketed specimen test assembly.

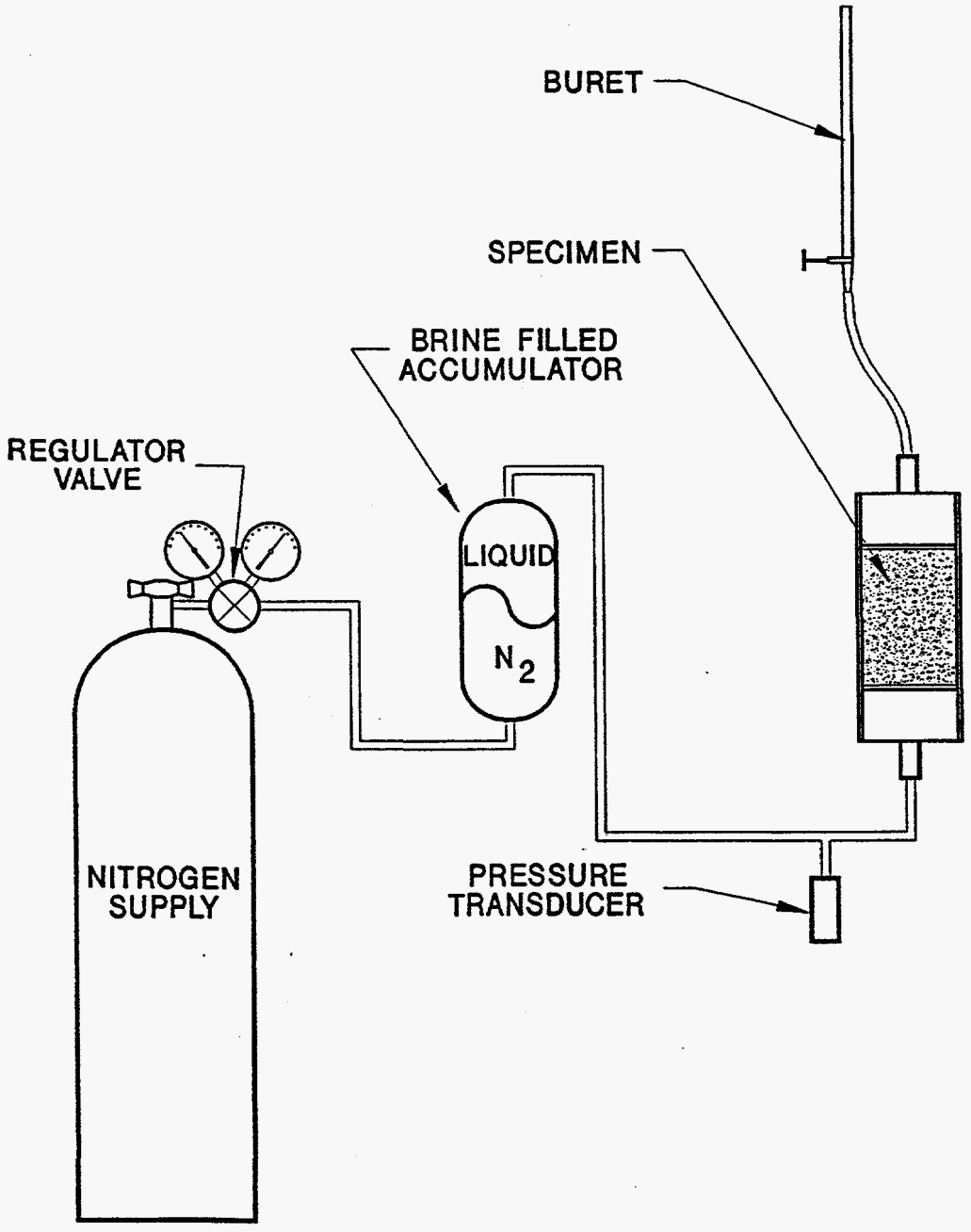

Figure 3-5. Brine permeability test setup.

along the jacket-specimen interface. In some cases where the flow rate was very high, the buret was periodically emptied during the test, and the amount emptied was recorded to calculate the accumulated flow quantity. In extremely high flow tests, the buret was removed entirely and replaced with a balance. The accumulated mass flow rate was then converted to a volume flow rate using the known density of brine (1.208g/cc [Brodsky, 1994]).

For those specimens tested with a gas permeant, the specimen assembly was connected to a rotameter flow meter system, as shown in Figure 3-6. Nitrogen gas was supplied to the flow meter by a pressurized bottle. The charge pressure to the flow meter was manually controlled with a valve located on the gas bottle, and measured by a pressure transducer located in the hydraulic line at the inlet to the flow meter. The flow meter consists of two components: an interchangeable flow tube and a tube holder. The design of the flow meter permits the removal of a tube with a specified maximum flow capacity and the replacement of the tube with another having either a larger or smaller flow capacity so that different flow rates can be accommodated with the same apparatus. The flow meter was hydraulically connected to the specimen using 3/16-inch i.d. stainless steel tubing. A second pressure transducer located in the hydraulic line near the inlet to the specimen provided the measurement for the specimen inlet gas pressure. Gas exiting the specimen was vented to atmosphere. Similar to the brine permeant tests, a hydrostatic stress of 1 MPa was applied to the external surface of the specimen. Then, the valve located on the pressurized nitrogen gas bottle was opened to permit the flow of nitrogen through the flow meter system and test specimen. The pressure at the inlet to the flow meter was adjusted to a value of 0.345 MPa (50 psi), which was the flow meter calibration pressure. The flow rate and gas pressure at the specimen inlet were then recorded by reading the flow meter and pressure transducer outputs, respectively.

Two of the specimens from the large-scale, dynamic-compaction blocks were subjected to a combination of hydrostatic compaction and hydrostatic creep consolidation loading. This loading caused the specimen fractional densities to increase from their initial value of about 0.9. As the specimens were deformed, nitrogen gas permeability measurements were conducted at incrementally higher levels of fractional density. The test system used for these tests was the same as the one described for the constant strain-rate tests, although a particular loading path was applied to the specimens. The loading history for a typical hydrostatic consolidation test can be summarized as follows:

1. A jacketed specimen was placed inside the pressure vessel of the testing machine and hydrostatically loaded to a stress of 1 MPa. A nitrogen gas permeability measurement was performed at this point.

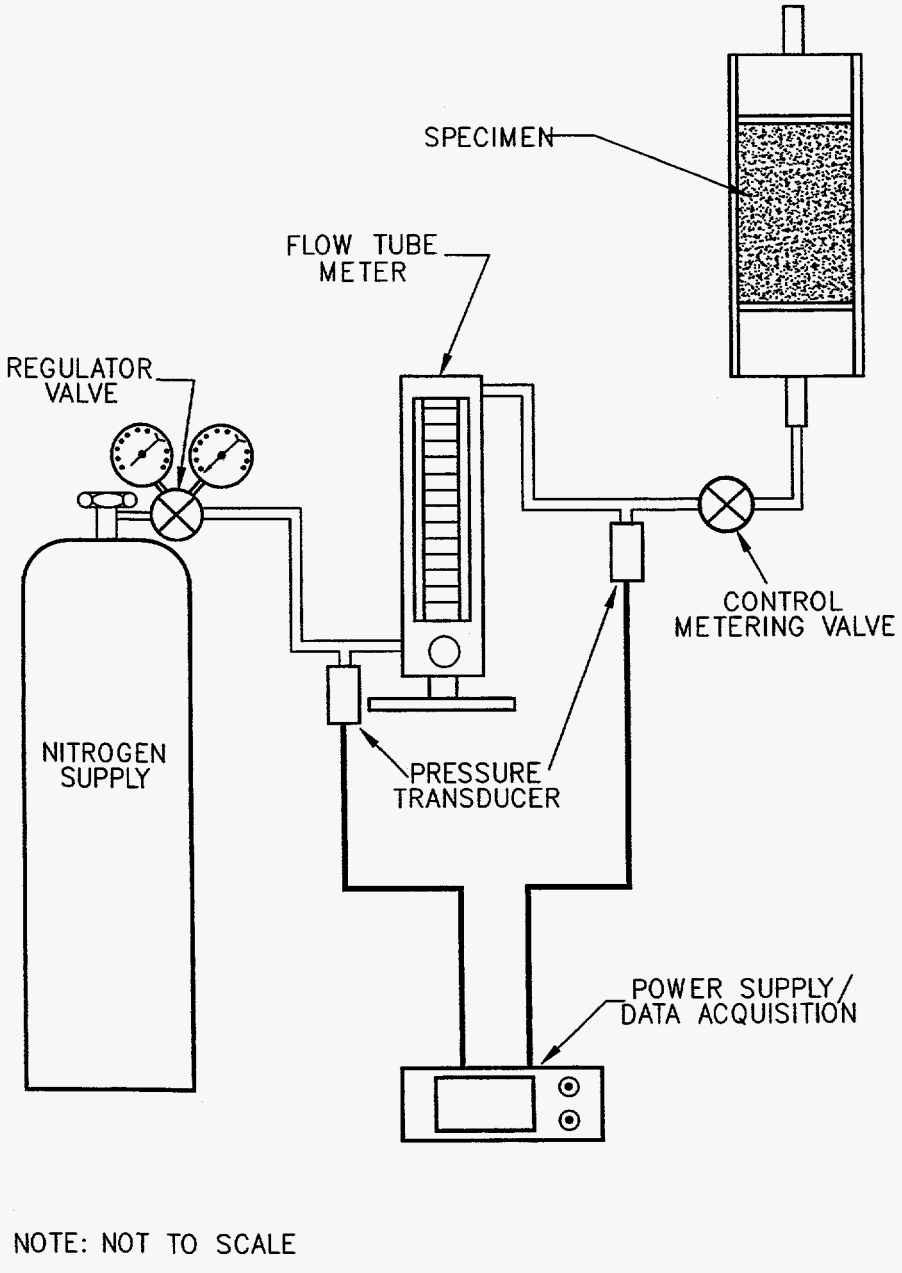

Figure 3-6. Gas permeability test setup.

2. The specimen was then hydrostatically loaded at a rate of 0.02 MPa/s. Loading continued until either of two criteria was met: (1) the fractional density had changed by a prescribed amount or (2) the hydrostatic stress had reached a prescribed level. If the first criterion was met, the specimen was unloaded to 1 MPa, reloaded to the highest stress it had attained during the hydrostatic loading stage, and then unloaded again to 1 MPa, at which time, another gas permeability measurement was performed. If the second criterion was met, the hydrostatic stress was held at its prescribed level until creep consolidation produced the desired change in fractional density. The specimen was then unloaded to 1 MPa, at which time another gas permeability measurement was performed. The hydrostatic unload-reload-unload cycle was performed to acquire data for calculating bulk modulus at the prescribed levels of fractional density.

3. Following the hydrostatic unload-reload-unload cycle and the gas permeability measurement, the specimen was subjected to a small, shear stress by increasing the axial stress to 6 MPa while maintaining the radial stress (i.e., confining pressure) at 1 MPa. The shear stress was then removed by lowering the axial stress to 1 MPa. Data collected during the shear loading/unloading were used to calculate values for Young's modulus and Poisson's ratio. Again, a gas permeability measurement was performed after the shear load cycle was completed.

4. Steps 2 and 3 were repeated until sufficient data were obtained to characterize the relationships between fractional density and gas permeability and elastic constants.

A typical load history for one specimen is shown in Figure 3-7. The load/unload cycles for both the hydrostatic and shear loading stages were of short duration (less than 1 hour), while the consolidation stages were often quite long (>5–6 days). Because the consolidation process was slow (particularly for dry specimens), hydrostatic stress levels were increased at later stages in the test so that density changes would occur more rapidly. The maximum hydrostatic stress level used to induce creep consolidation deformations was 15 MPa.

During the hydrostatic compaction/consolidation stages of the tests, current specimen density was determined from initial specimen dimensions and measurements of axial and radial strain taken during the test. Axial and radial deformations were measured using direct-contact extensometers as described previously for the constant strain-rate tests.

3.4 Petrographic Studies

Great care was taken to ensure consistency of test specimens. Specimens used in these laboratory experiments were derived from the large, dynamic-compaction demonstration initially and prepared in the laboratory later on. This section describes the microstructure of variously prepared specimens. Further descriptions are included in a memorandum included as Appendix A. In the end, consistency of grain size, moisture content, and starting density was obtained for all tested specimens. Because experimental results are controlled by these first-order specimen characteristics, features of the physical substructure are summarized here. Later in Section 4.4, petrofabrics of reconsolidated salt will be demonstrated via Scanning Electron Microscopy (SEM) and optical microscopy.

As noted earlier, several of these experiments were conducted on specimens prepared from the very large-scale, dynamic-compaction field demonstration conducted by Hansen and Ahrens. Only a few finished specimens were actually obtained from the blocks extracted from the large compacted mass. In addition to the limited number of test specimens, it was determined during the course of experimentation that the compacted mass had dehydrated from the original 1-percent water content. Therefore, it became necessary to produce alternative, similarly compacted samples in the laboratory to complete requisite experimental work.

RSI-325-96-034

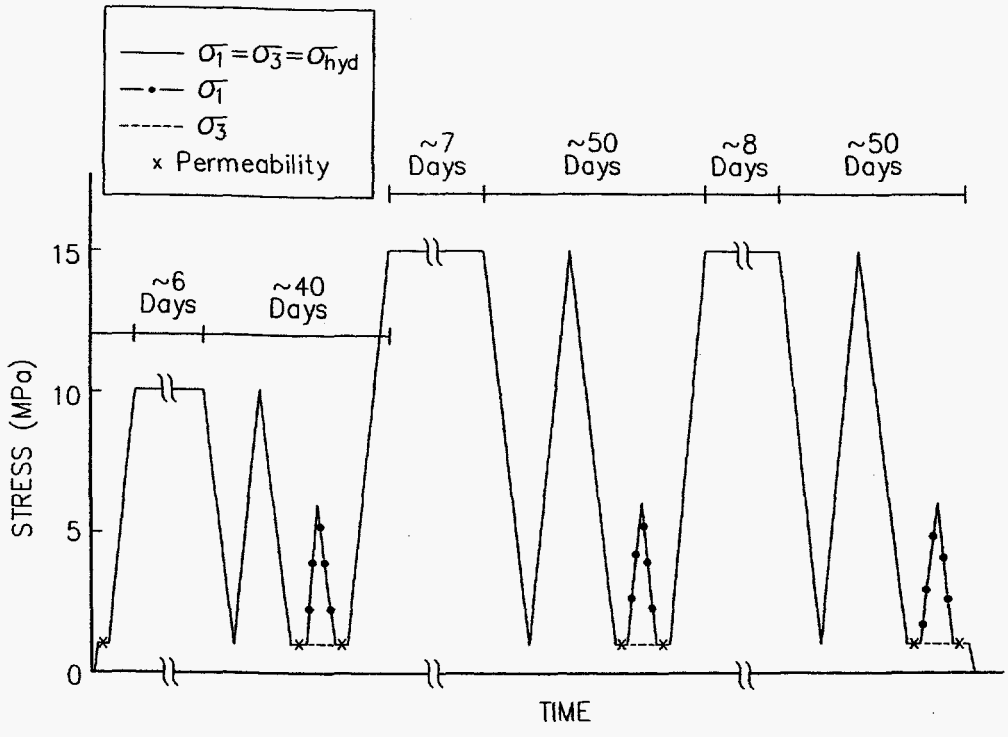

Figure 3-7. Typical load history for hydrostatic compaction and consolidation.

Specimens for SEM observations were all prepared by cutting down larger pieces into parallelepipeds having two dimensions approximately 20×20 millimeters. The sawn beam was then broken by finger pressure to produce a fresh face. This sample preparation technique was necessary because any other preparation technique, such as sawing or polishing, produces additional textures, obscuring the original. Comparisons here are made only for the substructure of the specimens before they are tested. Resultant microstructures of tested specimens are given in Section 4.4.

The characteristics of the compacted salt prepared by large-scale, dynamic compaction are examined first. Figure 3-8 (SEM numeric 0003) represents the mass of compacted grains magnified 1,100 times. Dynamically compacted salt aggregate structure has been examined and previously published (Hansen, 1997), and the heterogeneous gradation of fine particulate shown here is identical to those independent studies. Grain boundaries are open, and the relatively larger grains are abraded and blocky, rather more rounded than cleaved. Rounded abraded larger grains coupled with a significant population of fine grains indicate severe mechanical abrasion imparted by large-scale, dynamic compaction. Figure 3-9 (SEM numeric 0004) is the same material as above, shown at a magnification of only 110 times. One can observe a dense substructure comprising sorted grain sizes, with fine grains occupying available interstices.

Equivalent photomicrographs for laboratory-prepared test specimens are shown in Figures 3-10 and 3-11. At a magnification of 1,100, the ground mass comprises a well-cleaved, uniform grain size between 20 and 30 μm. Grain boundaries are open and the broken surface indicates a lack of intergranular cohesion, a feature very similar to the large-scale, dynamically compacted substructure. At 110 magnification, fine powder fills space between larger grains (up to 1 millimeter). At the lower magnification, little difference in size composition between the specimen preparation techniques can be seen.

These photomicrographs are representative of a larger population taken of several samples from the large-scale, dynamic-compaction demonstration and from laboratory-prepared samples. While laboratory-prepared samples are tailored to replicate the large-scale test fractional density (0.9) and can be prepared at an ideal water content, the texture of laboratory-prepared samples is different than that produced by large-scale, dynamic compaction. Both sample preparation processes produce a similar percentage of grains between 20 and 30 μm; however, the large-scale dynamic process produces a greater proportion of fines. Grains of laboratory-prepared specimens are cubic, as compared to more rounded, abraded grains produced by the full-scale demonstration. Based on knowledge of consolidation processes (that densification results from pressure solution/redeposition) the finer grain size produced by large-scale, dynamic compaction would be expected to increase consolidation rate relative to laboratory-prepared samples.

Other attempts to match laboratory-prepared samples to field-compacted samples were made. For example, one assembly used ten separate lifts. When the substructures of the three-lift samples, the ten-lift samples, and large-scale, dynamic compaction are compared, it is evident that the three-lift construction of test specimens is adequate for laboratory investigations (see Appendix A). Laboratory-prepared specimens are tailored to a desired moisture content, appropriate density, and a similar grain size, not withstanding the lack of fine grains. Further evidence on the adequacy of laboratory-prepared specimens is presented later when consolidated substructures are discussed.

RSI-325-98-156

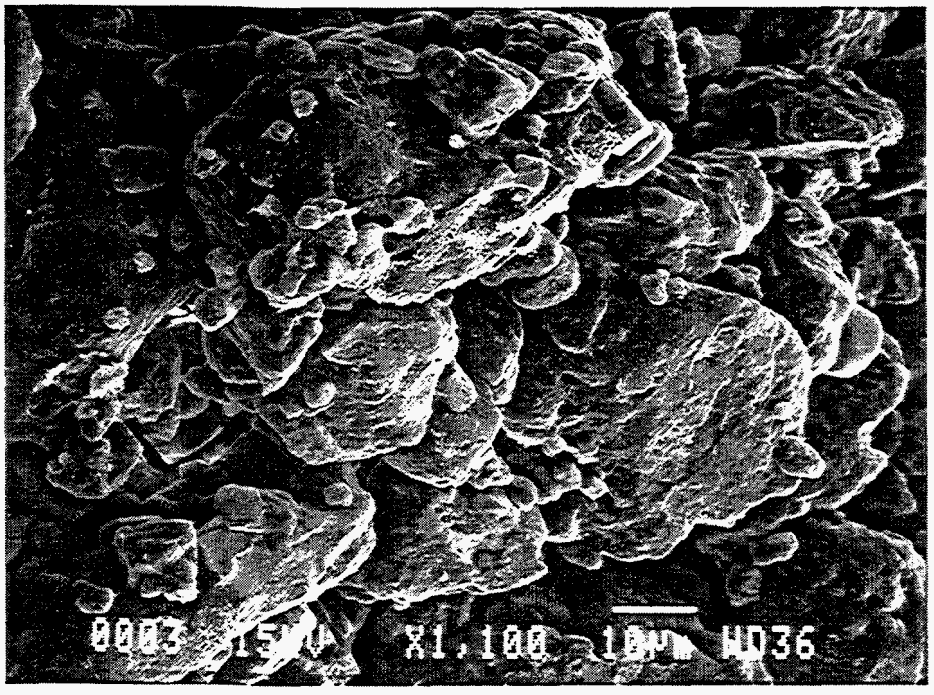

Figure 3-8. Compacted salt matrix from large-scale, dynamic-compaction demonstration (SEM 1,10X).

RSI-325-98-157

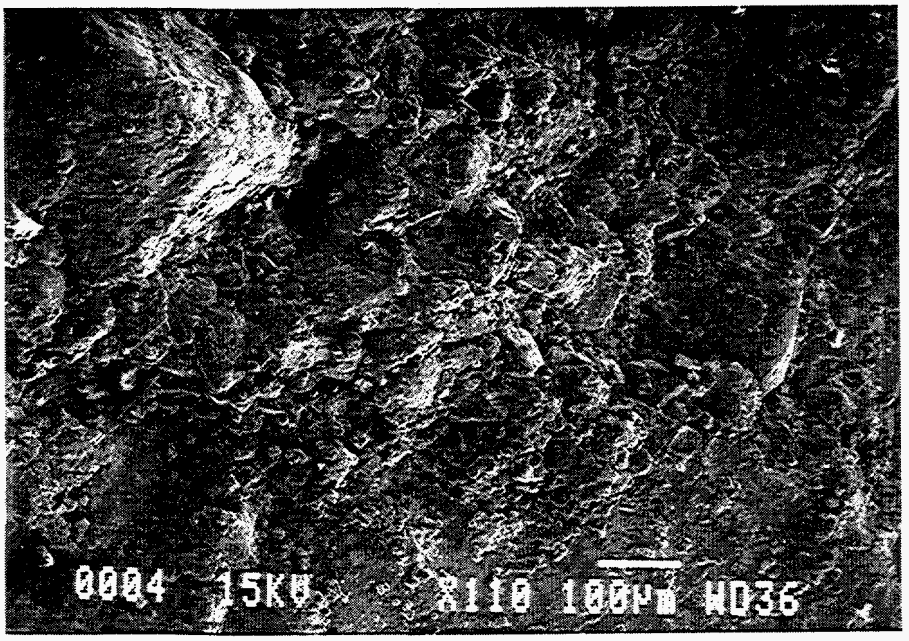

Figure 3-9. Compacted salt matrix from large-scale, dynamic-compaction demonstration (SEM 110X).

RSI-325-98-158

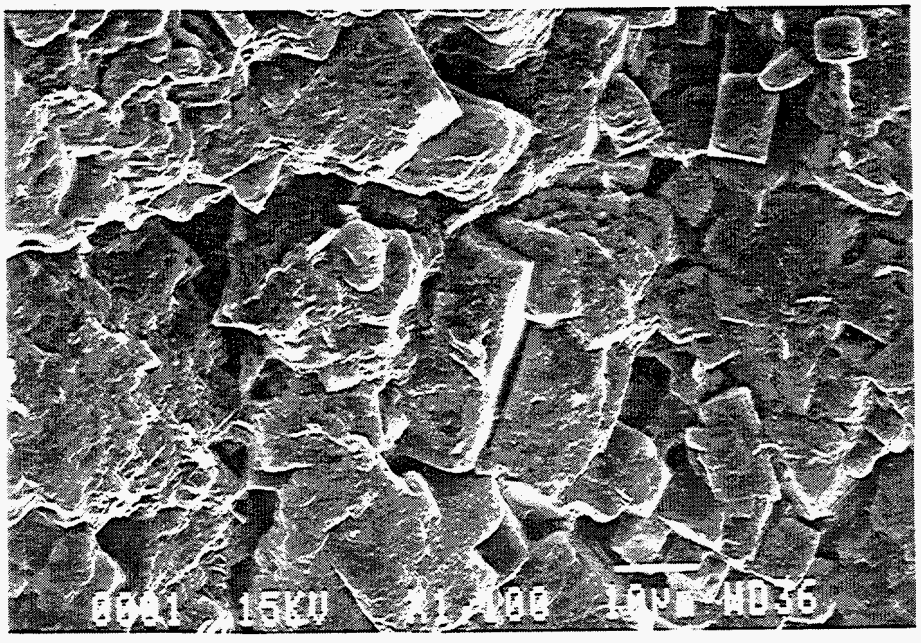

Figure 3-10. Compacted salt matrix from laboratory-prepared three-lift specimen. (SEM 1,100 X).

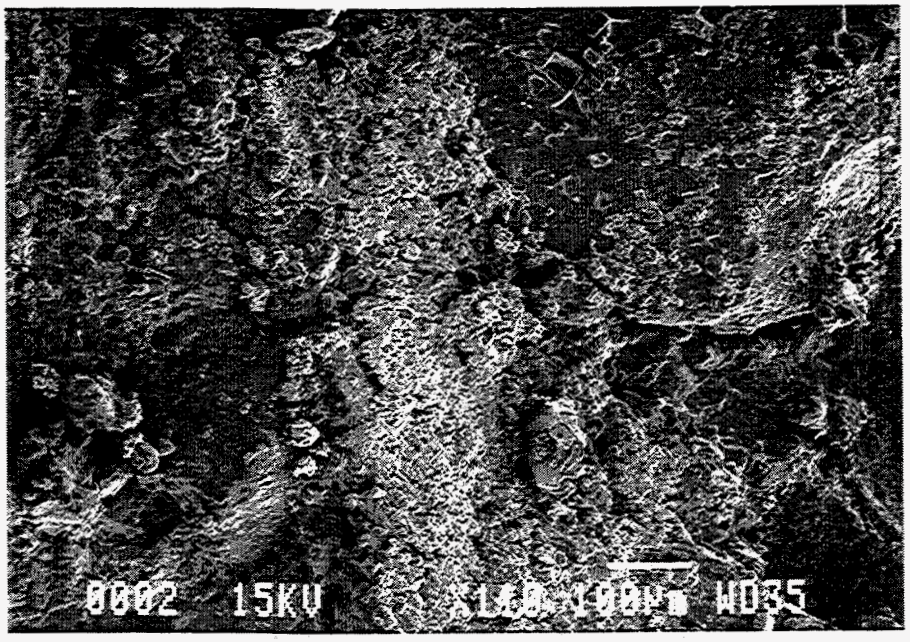

Figure 3-11. Compacted salt matrix from laboratory-prepared three-lift specimen (SEM 110X).

4.0 TEST RESULTS

The experiments conducted as part of this work comprised shear consolidation testing, constant strain-rate testing, and permeability testing. The results from each of these types of testing are reported in the individual sections that follow. One additional section presents the results of the petrographic studies carried out to provide a physical description of the densification mechanisms.

4.1 Shear Consolidation

A total of eight shear consolidation tests was performed; six were performed on laboratory-scale specimens manufactured at RE/SPEC, and two were performed on specimens cored from the large-scale samples provided by Hansen and Ahrens (1998). All tests were performed at a temperature of 25°C and an axial stress difference (axial stress minus radial stress) of 4 MPa. The only controlled variable that changed among the tests was the level of radial stress (confining pressure). The test matrix for the shear consolidation tests is shown in Table 4-1. The first column in the table contains the specimen identification. The following three columns give the axial stress, radial stress, and temperature, respectively. All tests were performed in a drained condition; i.e., the ends of the specimens were vented.

Table 4-1. Shear Consolidation Test Matrix

Specimen Identification	Test Conditions		
	Axial Stress (MPa)	Radial Stress (MPa)	Temperature (°C)
RS/DCCS/1	5	1	25
RS/DCCS/3	6	2	25
RS/DCCS/4	7	3	25
RS/DCCS/5	8	4	25
RS/DCCS/10	9	5	25
RS/DCCS/15	5	1	25
DCCS/3/2/3-1	8	4	25
DCCS/3/1/2-1	8	4	25

The data acquired during the test were used to calculate principal stresses and strains according to formulas that provided true stress and true strain measures. The sign convention was that positive values indicate compression. The data reduction formulas for axial and radial strain at each data point were:

$$\varepsilon_1 = -\ln\left(\frac{L_i}{L_o}\right) \tag{4-1}$$

$$\varepsilon_3 = -\ln\left(\frac{D_i}{D_o}\right) \tag{4-2}$$

where L_o and D_o are the original length and diameter of the specimen and L_i and D_i are the current length and diameter of the specimen at any data point.

The original specimen dimensions were those measured on the bench before the specimen was encased in its protective jacket. The current specimen dimensions were determined from the deformation measurements made during the test. The change in specimen length was calculated by correcting the LVDT measurements for nonspecimen deformation; the remainder represented the axial shortening of the specimen. The change in specimen diameter was calculated from the dilatometer data after correcting for movement of the axial force ram.

The data reduction formulas for calculating true stresses used the measurements provided by the load cell and pressure transducer, and accounted for the change in specimen area. The formulas for axial and radial stresses were:

$$\sigma_1 = \frac{F - P(A_r - A_s)}{A_s} \tag{4-3}$$

$$\sigma_3 = P \tag{4-4}$$

The variables F and P represent the measured values of total axial force and confining pressure, respectively. The current area of the specimen, A_s, was calculated using the previously determined radial strain values. The area of the loading ram, A_r, was constant.

The first five tests listed in Table 4-1 were designed to investigate the effect of changes in mean stress by testing at different confining pressures while holding the axial stress difference constant. The hypothesis was that a stress state would be encountered where the radial strain rate would initially be positive (consolidation) and then reverse direction and become negative as the specimen density increased. The creep strain results for these first five tests are compared in Figures 4-1 and 4-2, which plot axial creep strain and radial creep strain, respectively, as a

function of time. In Figure 4-1, the three axial strain curves for tests performed at confining pressure above 2 MPa exhibit an inflection where the axial strain rate begins to increase. This behavior appears to be repeatable and different from the three tests performed at confining pressure of 1 and 2 MPa. No explanation is offered for this apparent pressure-sensitive behavior, but the phenomenon is being noted as a point of interest.

A significant observation is apparent in Figure 4-2 where a trend appeared in the radial strain response; that is, the radial strain rate decreases as the confining pressure increases. A very significant phenomenon was observed in the tests performed at confining pressures of 4 MPa and 5 MPa. The radial strain rate in those two tests was initially positive (specimen diameter decreasing), and after some densification of the specimen, the radial strain rate decreased and ultimately changed sign (specimen diameter increasing). This observation supports the original hypothesis that the direction of the radial strain response depends upon both the state of stress being applied and the fractional density of the specimen.

The sixth test listed in Table 4-1 was performed to replicate the radial stress test condition imposed on the first test; i.e., a confining pressure of 1 MPa. The first test seemed to exhibit very large strains as compared to the strains measured for the tests performed at higher radial stresses, so a replicate test was conducted. The two tests performed at a radial stress of 1 MPa are compared in Figures 4-1 and 4-2. As seen in the figures, the results are very comparable. The strain response at 1 MPa may result from a different mechanism, such as translation/rotation of relatively loosely packed crystals. At the higher confining pressures, the grains would be more tightly packed and densification would be dominated by pressure solution/redeposition.

The last two tests listed in Table 4-1 were performed using specimens obtained from the large compacted mass provided by the Hansen and Ahrens demonstration. These two tests were conducted to estimate the specimen-to-specimen variability in the large-scale specimens and also to compare large-scale results with laboratory-scale results. The two tests from the large-scale blocks and the single test result from the laboratory-scale specimen are given in Figure 4-3. The same test conditions were applied to all three specimens; i.e., an axial stress difference of 4 MPa and a confining pressure of 4 MPa.

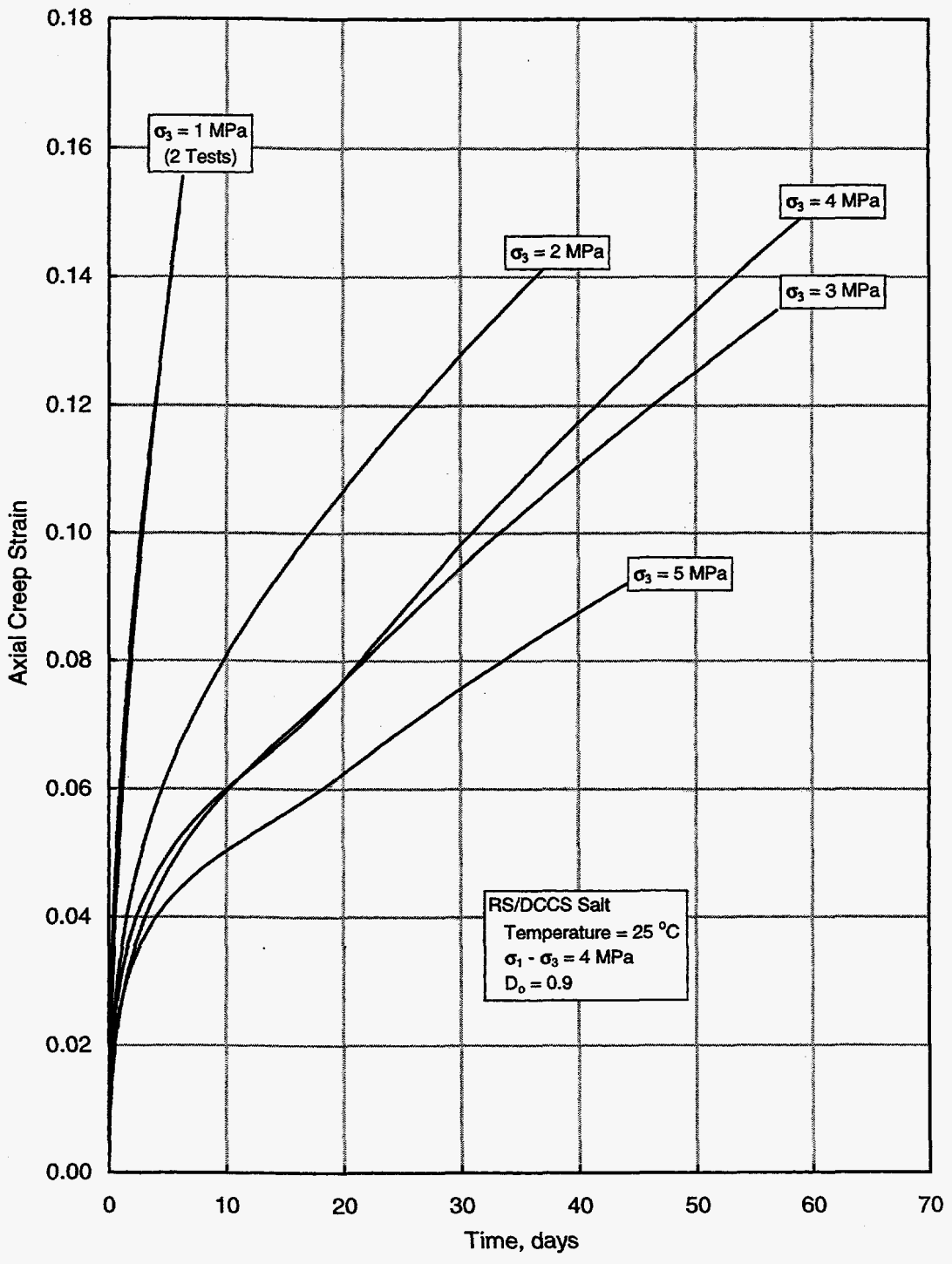

Figure 4-1. Axial creep strain as a function of time for laboratory-scale, dynamically compacted salt.

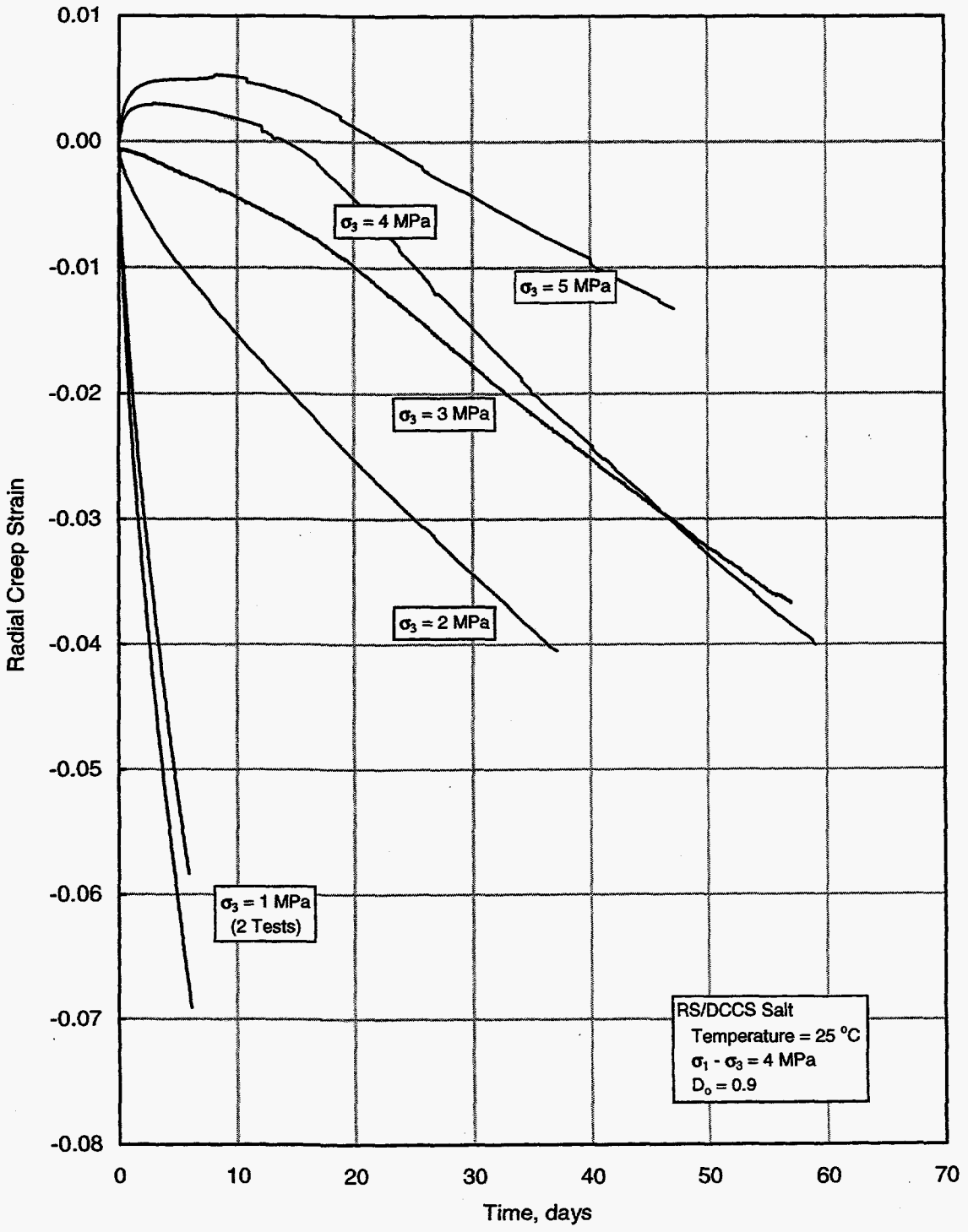

Figure 4-2. Radial creep strain as a function of time for laboratory-scale, dynamically compacted salt.

As seen in Figure 4-3, all three specimens displayed the same radial strain phenomenon; that is, the radial strain rate was initially compressive and then became extensile after some densification of the specimen. The difference between the laboratory-scale and large-scale results is likely caused by the difference in which the specimens were made. The large-scale specimens were cored from very large blocks, which were dynamically compacted as a single unit. Using that technique, it is expected that the particle size distribution of a specimen taken from the dynamically compacted mass is fairly homogeneous throughout the specimen volume. To the contrary, the laboratory-scale specimen was fabricated by dynamically compacting the crushed salt in three separate sections or lifts. This technique involved placing a third of the loose crushed salt in a mold and then compacting it by repetitive drops of a steel hammer. This process was repeated a second and third time to create a specimen of the proper length. The final product was a specimen that had two distinct zones (about ¼-inch thick) of fine crystals where the hammering took place that separated the specimen into three relatively homogeneous sections. During shear consolidation testing, the thin, fine-grain zones deformed differently than the three larger zones of coarser-grain crystals. This was apparent in post-test examination of the specimens where the fine-grain interface zones appeared as bulges. An example of the post-test profile of a typical specimen is given in Figure 4-4. The difference in deformation between the fine-grain and coarse-grain portions of the specimen was attributed to their probable difference in grain size. It is also possible that the fine-grain zones had a slightly higher fractional density at the outset. It is important to note that while the fine-grain zones may account for some difference between the laboratory-scale and large-scale results, the radial strain reversal phenomenon was observed in both types of specimens, as seen in Figure 4-3. This means that the radial-strain reversal should be seen in all types of crushed salt (assuming the proper stress state and fractional density) and is not just an experimental artifact.

Because of the post-test bulges seen in the laboratory-scale specimens, there was some concern that nonuniform deformation might have caused significant errors in the strain measurements made during the test. This concern was addressed by comparing the total inelastic strain measured during the test (the sum of stress application strains and constant stress consolidation strains) to the strain calculated as the logarithm of the ratio of post-test dimension to pre-test dimension. Those comparisons are outlined in Table 4-2 and indicate that the test system measurements were accurate. The axial strain values compare extremely favorably. The radial strain values do not compare as well as the axial strain values. This difference may be caused by the technique used to measure the specimen diameter. Two orthogonal measurements of diameter were made at 13 points along the length of the specimen. These values were then averaged to give an average specimen diameter that was used for the bench measure strain calculation. The bulges in the specimen could have a disproportionate effect on the average diameter determination, depending upon the exact locations where the measurements were made.

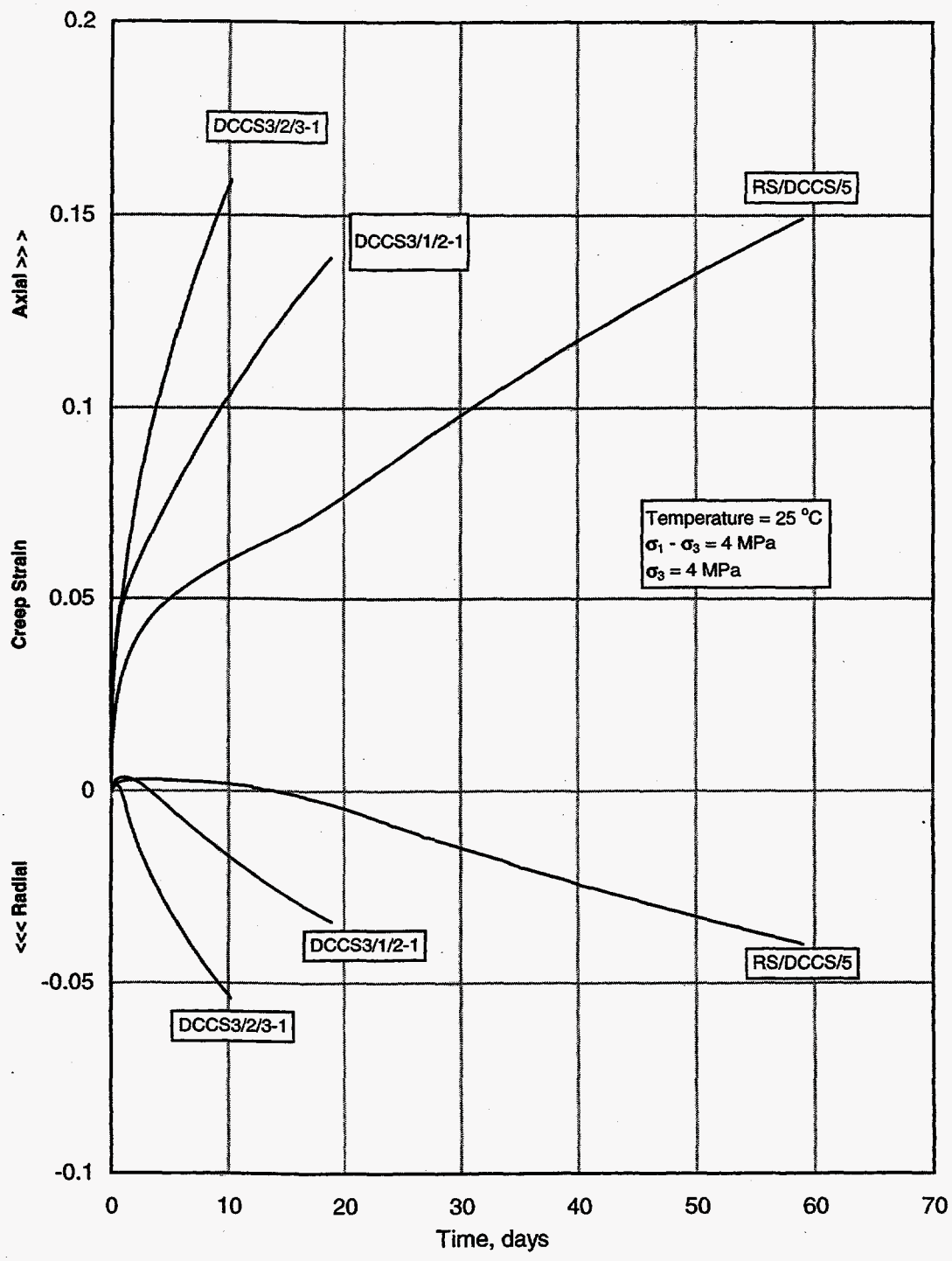

Figure 4-3. Comparison of test results from large-scale and laboratory-scale dynamically compacted salt specimens.

The effect of the bulges would be to introduce a bias in the diameter measurement, such that the post-test diameter would be overestimated, leading to an overestimation of radial strain in the bench measure calculations. Another possible explanation for the difference in radial strain measures is the existence of a leak in the test system dilatometer. A leak would cause the test measurements to underestimate the radial strain during the test. No gross leaks were detected during testing, but a small dilatometer leak could cause the relatively small differences in radial strain noted in Table 4-2.

Table 4-2. Comparison of Test System and Bench Strain Measurements

Specimen I.D.	Principal Strain Direction	Load Path Segments			Test System Total	Bench Measure Total
		Hydrostatic Pressurization	Shear Stress Application	Creep Consolidation		
RS/DCCS/1	ε_1	(a)	0.00192	0.15550	0.15742+	0.16763
	ε_3	(a)	–0.00084	–0.06905	–0.06989+	–0.06335
RS/DCCS/3	ε_1	0.00153	0.00187	0.16541	0.16882	0.16981
	ε_3	0.00153	–0.00069	–0.04976	–0.04891	–0.05294
RS/DCCS/4	ε_1	0.00967	0.00181	0.14565	0.15712	0.15238
	ε_3	0.00967	–0.00062	–0.04342	–0.03437	–0.04442
RS/DCCS/5	ε_1	0.00349	0.00166	0.14917	0.15432	0.15507
	ε_3	0.00349	–0.00234	–0.04005	–0.03890	–0.04102
RS/DCCS/10	ε_1	0.00362	0.00109	0.09518	0.09989	0.09544
	ε_3	0.00362	–0.00026	–0.01324	–0.00989	–0.01467
RS/DCCS/15	ε_1	0.00214	0.00152	0.15064	0.15431	0.15290
	ε_3	0.00214	–0.00046	–0.05835	–0.05666	–0.06260

(a) No deformation data collected. The total system strain should have some small compressive strain added. Note that the effect would make the test system measurement lie closer to the bench measurement values.

At the termination of seven of the eight tests on dynamically compacted crushed salt, an unload/reload cycle was conducted. The data collected during the reload portion of the cycle were used to calculate estimates of the elastic constants. The data analysis was relatively simple. The slope of the axial stress difference versus axial strain curve represented Young's modulus, E. Poisson's ratio, ν, was estimated by calculating the ratio of Young's modulus to the slope of the axial stress difference versus radial strain curve. Using the estimates of E and ν, an estimate of bulk modulus, K, was then calculated from the relation $K = E / [3(1-2\nu)]$. The suite of elastic constants determined in this fashion is shown in Table 4-3. The first column contains the specimen identification and the next three columns list the elastic constant estimates. The final column lists the fractional density of the specimen at the time the unload/reload cycle was conducted.

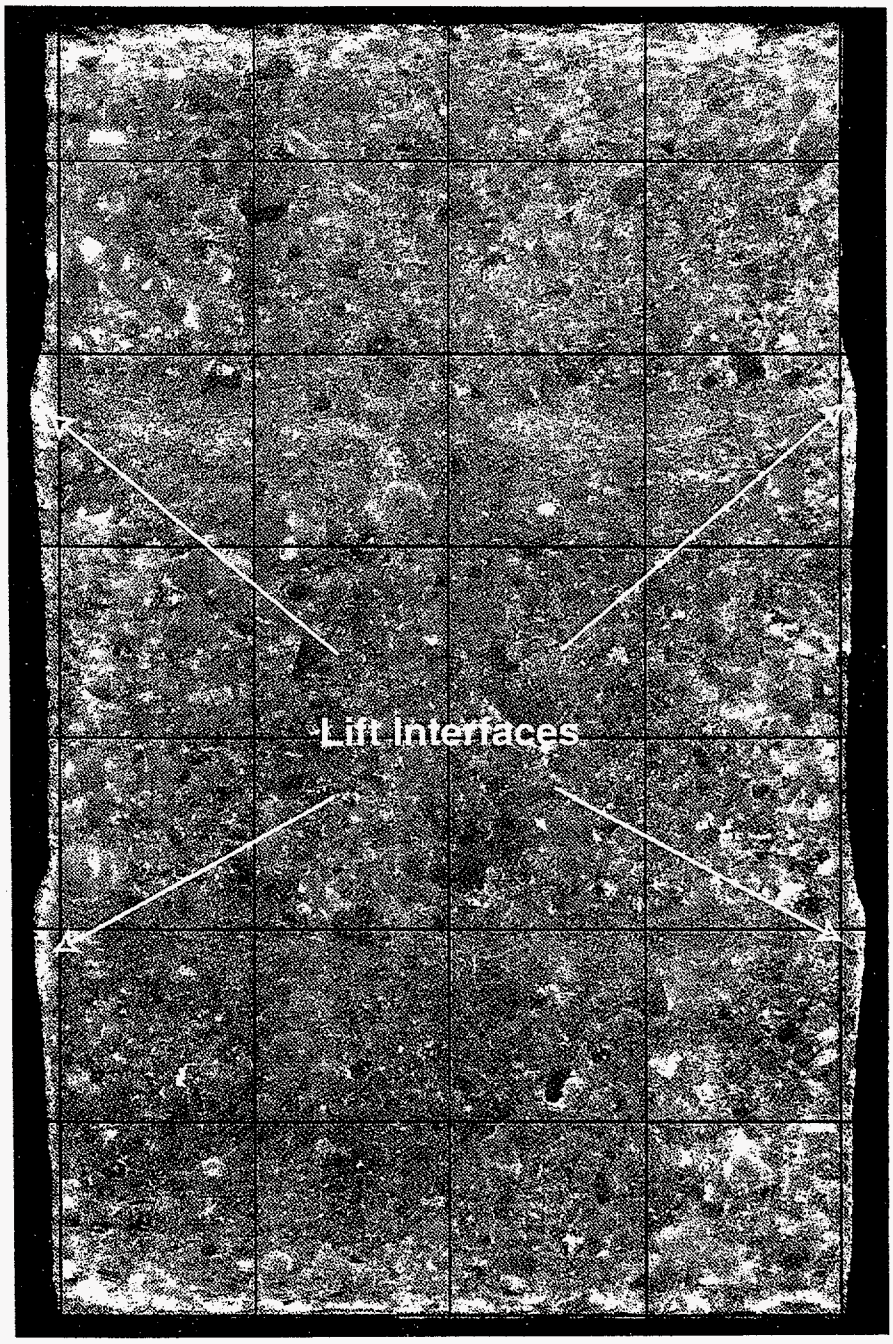

Figure 4-4. Polished half cylinder of consolidated three-lift specimen.

An inspection of the values given in Table 4-3 indicates that the elastic constants display a dependence upon the value of the fractional density of the specimen. This dependence is analyzed later at the end of Section 4.3 on permeability because additional elastic constant results were obtained during that testing.

Table 4-3. Elastic Constants for Dynamically Compacted Crushed Salt

Specimen I.D.	Young's Modulus, E (GPa)	Poisson's Ratio, ν	Bulk Modulus, K (GPa)	Fractional Density
RS/DCCS/1	N/A	N/A	N/A	N/A
RS/DCCS/3	11.7	0.303	9.9	0.971
RS/DCCS/4	13.0	0.480[(a)]	108.0	0.988
RS/DCCS/5	11.7	0.339	12.1	0.969
RS/DCCS/10	12.6	0.386	18.4	0.982
RS/DCCS/15	6.3	0.330	6.1	0.939
DCCS3/2/3-1	9.5	0.368	12.0	0.971
DCCS3/1/2-1	12.1	0.291	9.6	0.994

(a) Apparent outlier. Causes a gross increase in bulk modulus value.

4.2 Constant Strain Rate

Three constant strain-rate tests were performed on laboratory-scale specimens. The specimens were dynamically compacted using the same technique and raw crushed-salt materials that were employed for fabrication of the shear consolidation specimens. Thus, the constant strain-rate specimens had a nominal length of 200 millimeters, a nominal diameter of 100 millimeters, and a nominal fractional density of 0.9. All three tests were performed at a confining pressure of 1 MPa, a temperature of 20°C, and a constant axial strain rate. The constant axial strain rate was different for each test, as shown in Table 4-4, which is the completed test matrix. The data acquired during the tests were used to calculate principal stresses and strains according to formulas that provided true stress and true strain measures, as described for the shear consolidation tests. The sign convention was also the same; positive values indicate compression.

Table 4-4. Test Matrix for Constant Strain-Rate Experiment

Specimen I.D.	Axial Strain Rate (10^{-7} s^{-1})	Confining Pressure (MPa)	Temperature (°C)
RS/DCCS/11	0.5	1	20
RS/DCCS/6	1.0	1	20
RS/DCCS/21	2.0	1	20

Specimen RS/DCCS/6 was used to perform the first constant strain-rate test on crushed salt, and this first test served to refine the procedure outlined previously in Section 3.2.3. The first two attempts at performing this test were aborted, but the third attempt was successful and is being reported here. The first attempt was aborted because the constant strain-rate phase of the test was entered before the consolidation rates in the preceding hydrostatic phase had slowed to a value less than 1×10^{-7} s^{-1}. This caused the system to unload, as described in Section 3.2.3. The second attempt was aborted by failure of an electronic power supply in the test system shortly after the constant strain-rate phase had begun.

After determining new specimen dimensions (there was some deformation induced during the first two aborted attempts), a third attempt was successful. At the start of the third attempt, the specimen had a length of 190.3 millimeters, a diameter of 101.6 millimeters, and a fractional density of 0.92. The test duration was about 1 week, and the controlled test variables were maintained at a constant pressure of 1 MPa and a constant axial strain rate of 1×10^{-7} s^{-1} as shown in Figure 4-5 that plots the measured stresses and strains as a function of time. The plot origin represents the first data point acquired before any stresses were applied. Thus, the plot represents the entire loading history of the specimen, including the initial hydrostatic ramp up to the confining pressure of 1 MPa, the hydrostatic consolidation stage, and then the shear loading conducted at a constant axial strain rate. During the hydrostatic loading, axial strain exceeded radial strain. During the shear loading phase of the test, a small increase in compressive radial strain was measured, followed by extensile radial strains as loading continued. This appears to be a different radial strain behavior than was observed during shear consolidation creep testing at a confining pressure of 1 MPa. The fact that a small amount of compaction was observed during the initial constant strain rate shear loading may be attributed to the fact that at early loading times, the stress differences are small; whereas, in the creep tests the stress difference was 4 MPa.

The discontinuities in the axial stress measurement were traced back to a test system control problem. A multirange signal conditioner was used to measure the axial strain and that signal conditioner was adjusted for maximum sensitivity at the start of the test. As the axial strain increased, the system automatically changed to a less sensitive range. During this range switch, the closed-loop feedback circuitry is designed to operate in a "bumpless transfer" fashion; however, the system was not well tuned for these tests and a small error was introduced into the control signal during the range switch. This problem was eventually diagnosed and eliminated, but not until after all three tests in Table 4-4 were conducted, so the discontinuities in axial stress were seen in all three tests.

The other two constant strain-rate tests, RS/DCCS/11 and RS/DCCS/21, were performed without incident at axial strain rates of half and double, respectively, the strain rate used for RS/DCCS/6. The results from these two tests are shown in Figures 4-6 and 4-7, which plot the entire load history of the tests as a function of time.

The results from the three tests are compared in Figure 4-8, which plots the axial stress response from each test as a function of time. As expected, the axial stress rate is highest for the test conducted at the highest strain rate. The entire load history is plotted for each test, so they do not all start at the same point in time near the origin because of the differences in the hydrostatic consolidation duration.

Figure 4-9 plots the axial stress response of each specimen as a function of the specimen fractional density. The fractional density of the specimens was calculated using the volumetric strain data as:

$$D = \frac{\rho}{\rho_{\max}} = \frac{\rho_o}{\rho_{\max}(1-e_v)} \tag{4-5}$$

D is the fractional density, ρ is the current density, ρ_o is the density at the start of the test, ρ_{max} is the density of intact salt, and e_v is the engineering volumetric strain. For these calculations, the density of intact salt was 2.16 g/cc.

As seen in Figure 4-9, the axial stress response depends primarily on the fractional density of the specimen. The expectation was that a different response would be seen among the different strain-rate conditions. The fact that no large difference is seen may be attributable to the relatively small range of strain rates that was investigated.

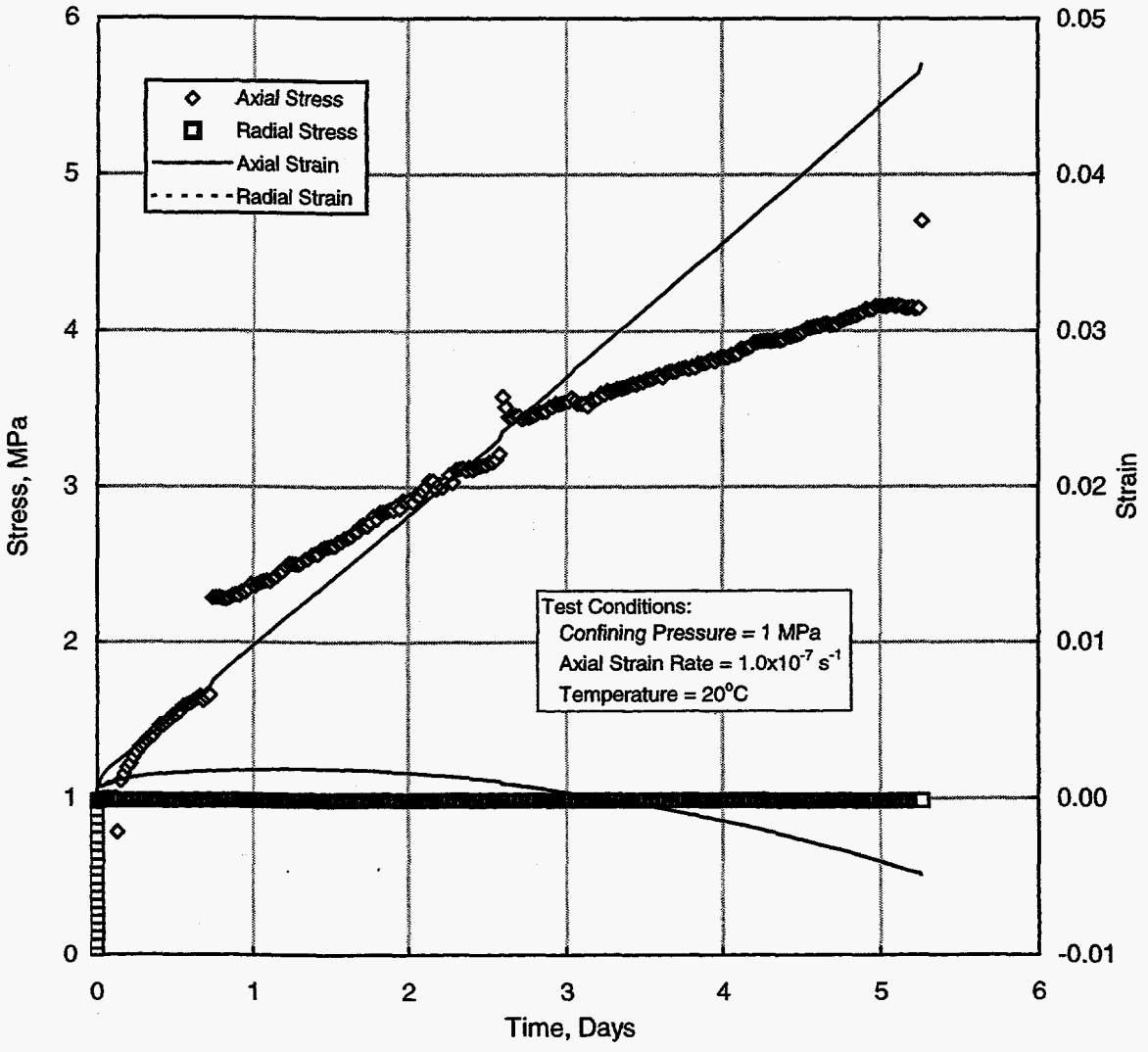

Figure 4-5. Constant strain-rate test on specimen RS/DCCS/6.

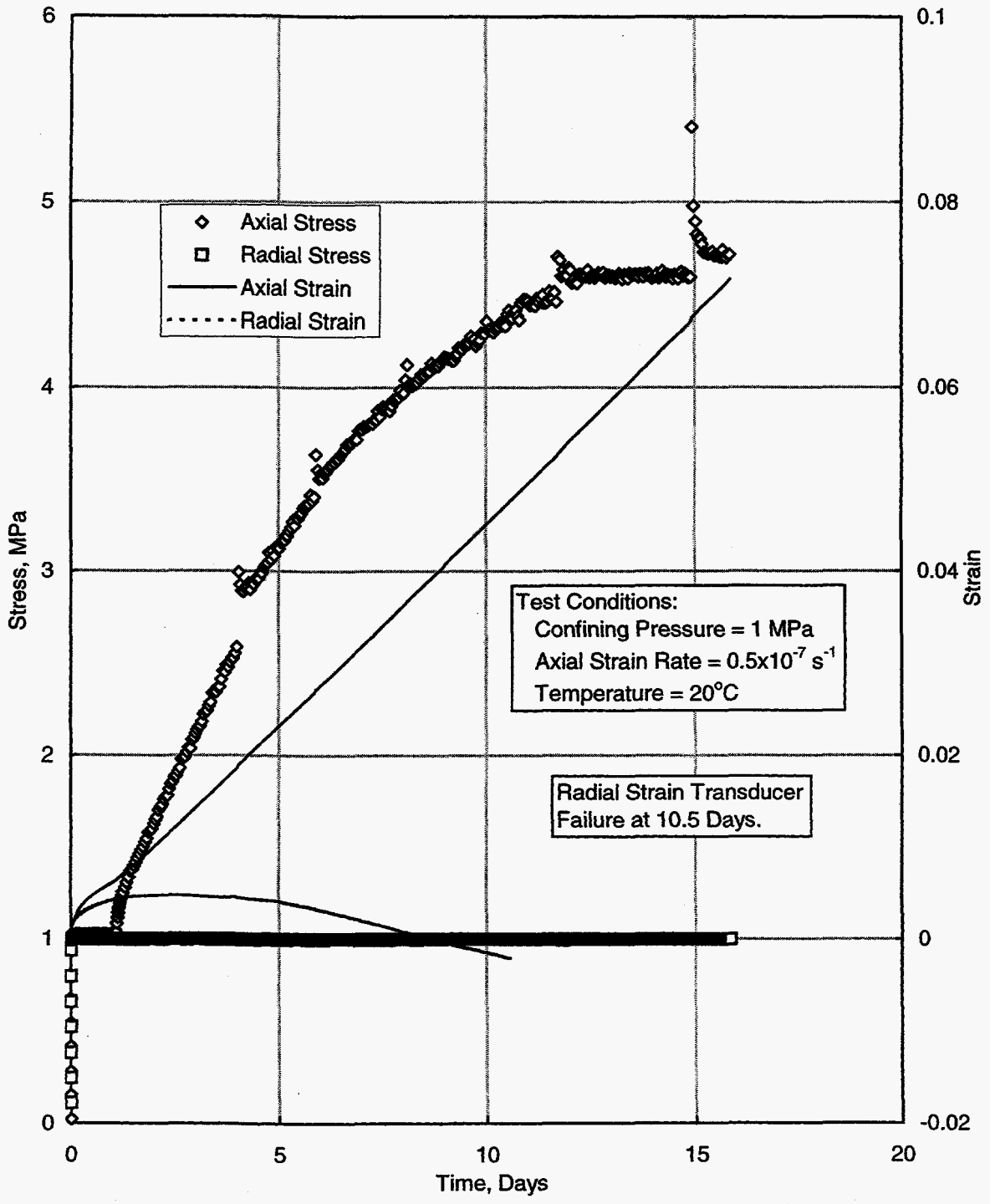

Figure 4-6. Constant strain-rate test on specimen RS/DCCS/11.

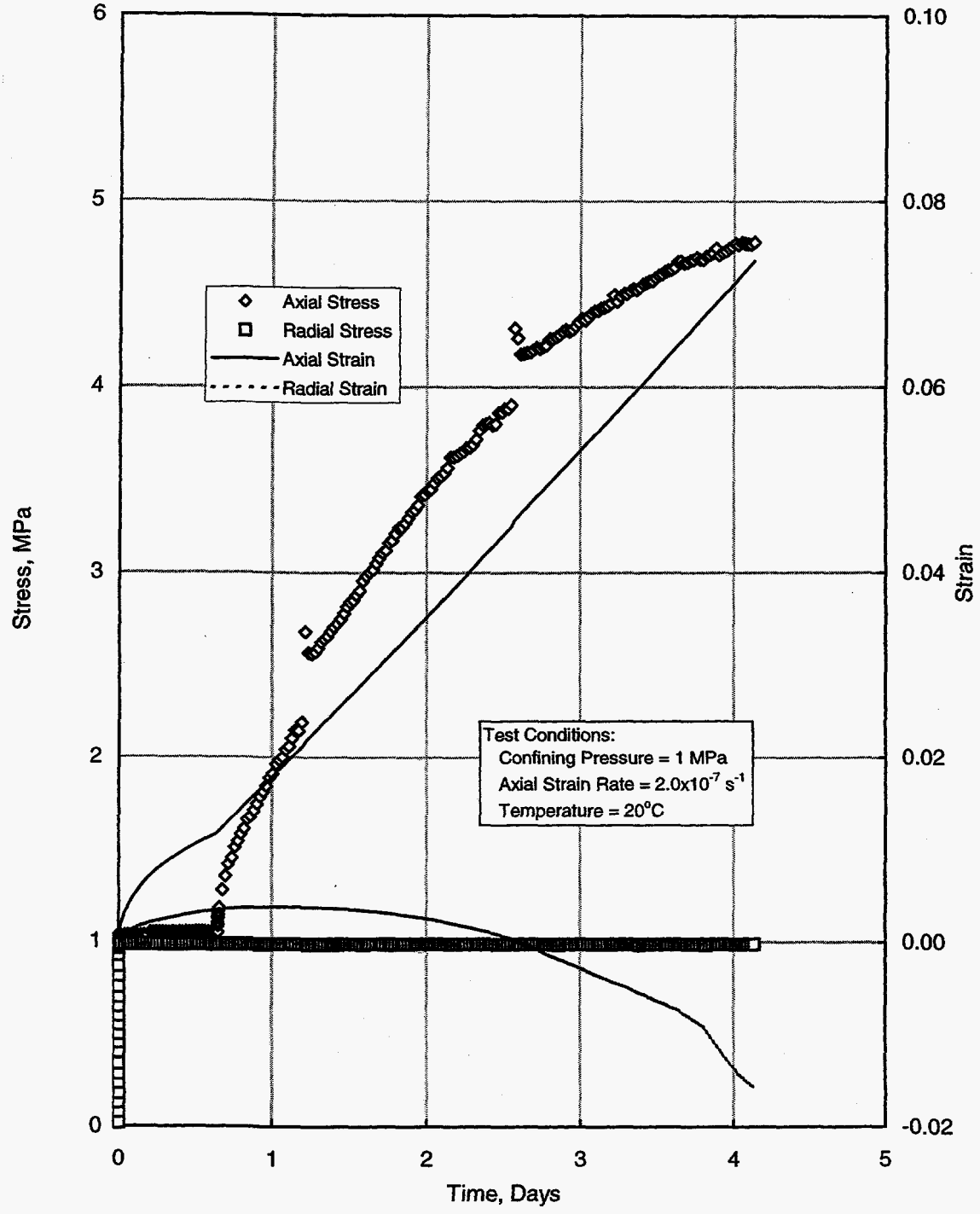

Figure 4-7. Constant strain-rate test on specimen RS/DCCS/21.

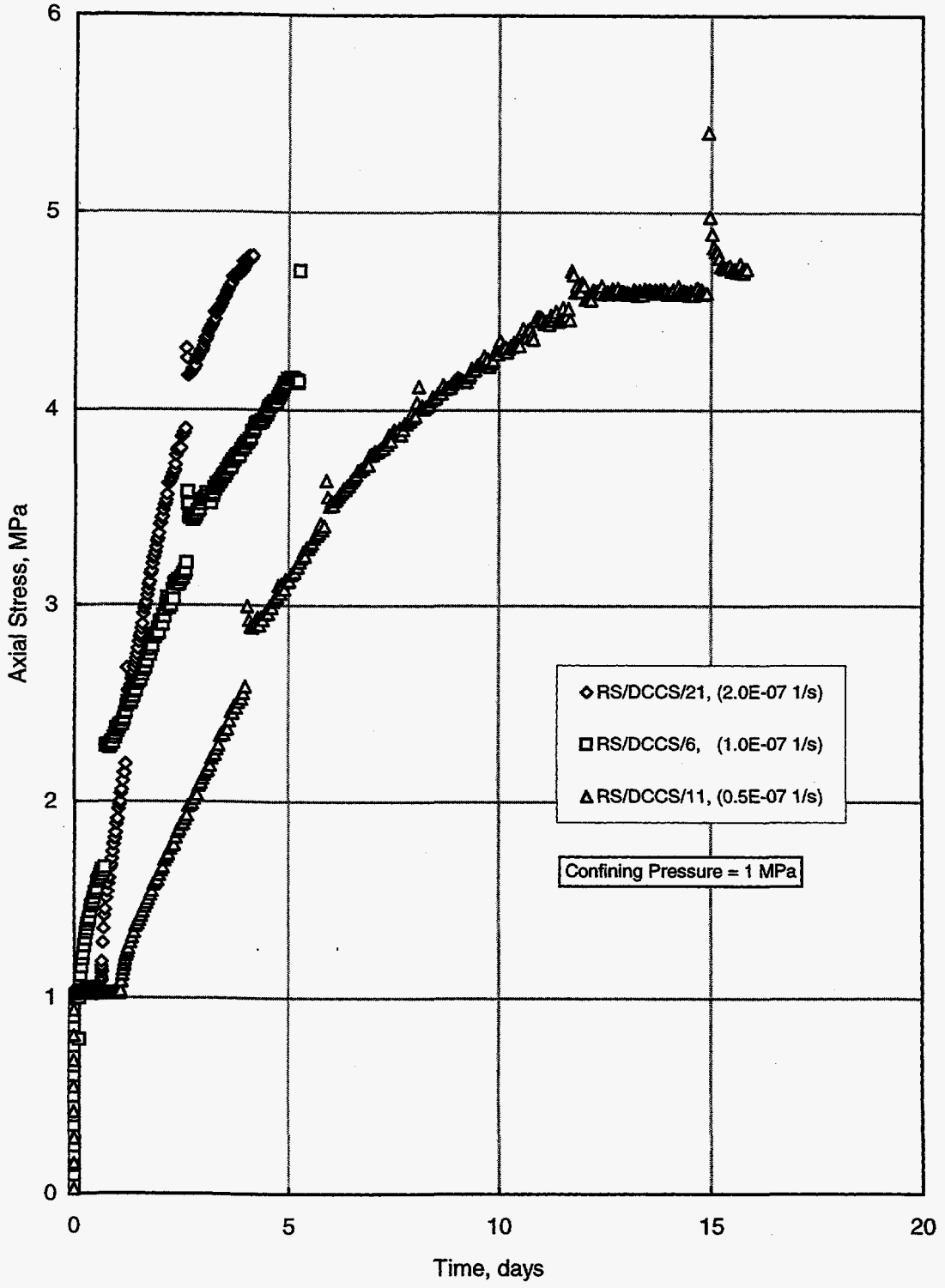

Figure 4-8. Comparison of results from three constant strain-rate tests.

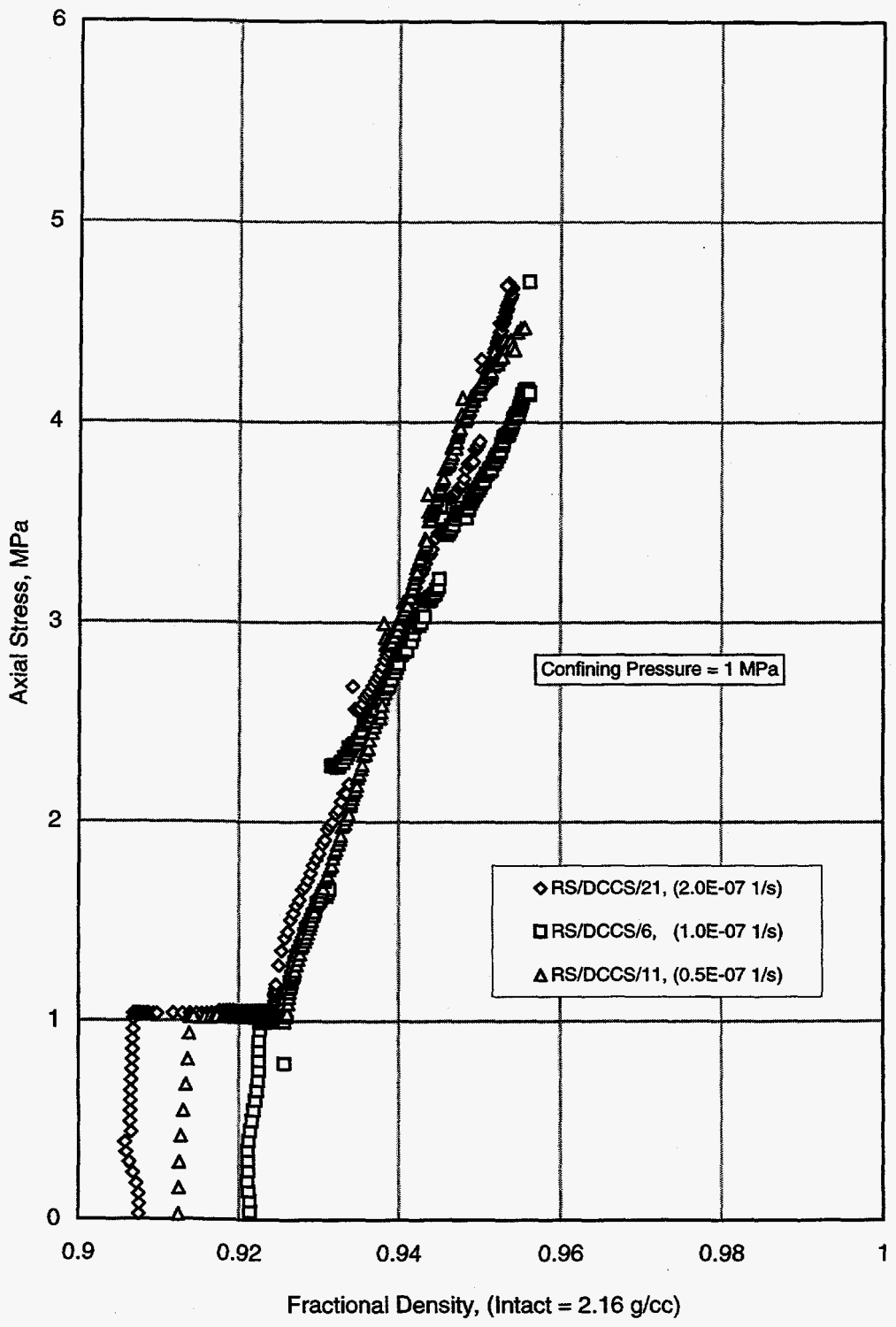

Figure 4-9. Axial stress response as a function of fractional density for three constant strain-rate tests.

4.3 Permeability

Three brine permeability tests were performed on specimens that had been previously tested for permeability using nitrogen gas. The current tests were performed at a temperature of 25°C using a hydrostatic confining stress of 1 MPa and a pore pressure of 0.345 MPa to drive the brine permeant. These test conditions were comparable to those used previously when the specimen permeability was determined using nitrogen gas as the permeant. The data reduction was based on Darcy's law as outlined by Brodsky (1994):

$$k = \frac{Q\mu L}{A\Delta P} \tag{4-6}$$

where:

k = permeability
Q = measured flow rate of brine
A = cross - sectional area of specimen
μ = brine viscosity = 1.26cP (Brodsky, 1994)
L = current specimen length
ΔP = pressure drop across the specimen.

The matrix of tests is presented in Table 4-5. The first column in the table identifies the specimen. The second and third columns contain the test conditions. The fourth column is the fractional density of the specimen at the start of the test, and the fifth column is the permeability value calculated for each specimen.

Table 4-5. Summary of Brine Permeability Experiment

Specimen I.D.	Test Conditions		Initial Fractional Density	Permeability (m^2)
	Confining Pressure (MPa)	Brine Inlet Pressure (MPa)		
DCCS/3/3/3-1	1	0.35	0.90	0[(a)]
CS/DC2/T2S-1/1	1	0.35	0.86	8.2×10^{-14}
CS/DC1/8-3	1	0.35	0.86	1.5×10^{-14}

(a) This test had an initial permeability of about 5×10^{-16} m^2. As the test progressed, the specimen consolidated and the permeability decreased to near zero.

The test on DCCS3/3/3-1 produced the data shown in Figure 4-10 that plots volumetric strain as a function of time on the primary axis and brine permeant flow as a function of time on the secondary axis. Two of the four curves in Figure 4-10 are actual test measurements; the other two are calculated. The curve labeled *Buret Measurement* is the total measured volume of brine collected at the vented end of the specimen, and the curve labeled *Volumetric Strain* is a test system measurement provided by the dilatometer. The data indicate that the saturated specimen was consolidating; thus, some volume of brine was getting expelled at the vented specimen end. This means that the buret measurement had two components. One was the volume of fluid being expelled by the action of consolidating the specimen, and the other was the volume of fluid traveling through the specimen from the pressurized brine inlet at one end of the specimen to the vented specimen end where the buret was located. Figure 4-10 implies that permeability decreases as fractional density increases. Such a relationship is reasonable, but other factors can also affect permeability without a change in fractional density. For example, under constant conditions, Brodsky (1993) reported decreasing brine permeabilities that were probably attributable to localized precipitation.

The curve labeled *Calculated Consolidation Flow* is the volume of fluid expelled from the specimen, which was calculated from the volumetric strain data. This calculation was performed by first using the relationship from Brodsky (1993) describing how the specimen density changes as a function of volumetric strain:

$$\rho_i = \rho_o \times \left(\frac{1}{1-\varepsilon_v} \right) \tag{4-7}$$

where ρ_i is the current density of the specimen, ρ_o is the original (pretest) density of the specimen, and ε_v is the engineering volumetric strain which is signed positive for compression. A second equation relates the pore space volume to the fractional density of the specimen:

$$PV_i = V_o \times \left(1 - \frac{\rho_i}{\rho_{\max}} \right) \tag{4-8}$$

PV_i is the pore space volume, V_o is the original volume of the specimen, and ρ_{max} is the density of intact salt. The ratio of the two densities is known as the fractional density of the specimen. Substituting the first equation into the second gives a relationship for the change in pore space volume as a function of the volumetric strain:

$$PV_i = V_o \times \left(1 - \frac{\frac{\rho_o}{\rho_{\max}}}{1-\varepsilon_v} \right) \tag{4-9}$$

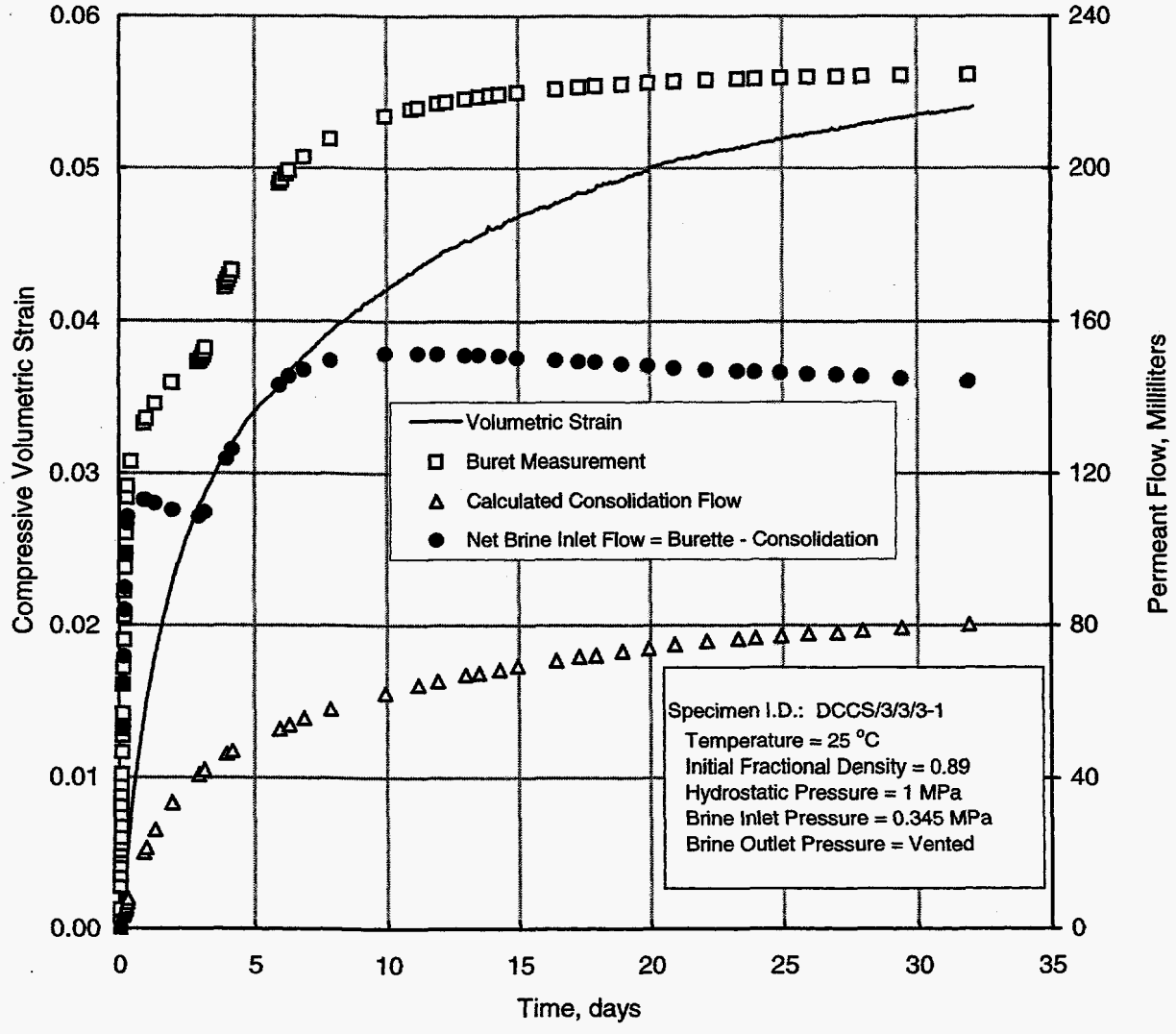

Figure 4-10. Volumetric strain and brine flow as a function of time for specimen DCCS3/3/3-1.

The curve labeled *Calculated Consolidation Flow* is the volume of fluid expelled from the specimen, which was calculated from the volumetric strain data. This calculation was performed by first using the relationship from Brodsky (1994) describing how the specimen density changes as a function of volumetric strain:

$$\rho_i = \rho_o \times \left(\frac{1}{1-\varepsilon_v} \right) \tag{4-10}$$

where ρ_i is the current density of the specimen, ρ_o is the original (pretest) density of the specimen, and ε_v is the engineering volumetric strain which is signed positive for compression. A second equation relates the pore space volume to the fractional density of the specimen:

$$PV_i = V_o \times \left(1 - \frac{\rho_i}{\rho_{\max}} \right) \tag{4-11}$$

PV_i is the pore space volume, V_o is the original volume of the specimen, and ρ_{max} is the density of intact salt. The ratio of the two densities is known as the fractional density of the specimen. Substituting the first equation into the second gives a relationship for the change in pore space volume as a function of the volumetric strain:

$$PV_i = V_o \times \left(1 - \frac{\frac{\rho_o}{\rho_{\max}}}{1-\varepsilon_v} \right) \tag{4-12}$$

Because the specimen was saturated, the volume of expelled pore fluid was calculated as the change in specimen pore volume. The volume of expelled fluid was then subtracted from the buret measurement to get the curve labeled *Net Brine Inlet Flow*. This net brine flow was the value used to calculate permeability. From inspection of the figure, it is apparent that the permeability rapidly decreased to a final value of about zero. Actually, the curve shows a small negative slope that was attributed to a combination of small measurement errors. Another possibility was that a pore pressure built up in excess of the 0.345 MPa pressure used to drive the brine through the specimen; however, such an increase would require that the vented end of the specimen was somehow plugged. The possibility of a plugged vent was checked by slowly lowering the hydrostatic confining pressure from its 1 MPa value to the 0.35 MPa brine inlet pressure value. The pressure was dropped at a rate of 0.1 MPa/minute while the buret was monitored for a change in the level of brine. The brine level remained constant until the confining pressure had decreased to the 0.35 MPa brine inlet pressure, at which time, the brine began flowing along the specimen-to-jacket interface and the buret reading began to increase. Since the brine level in the buret remained constant until the confining pressure was low enough to allow flow along the specimen-to-jacket interface, the conclusion was that the upper pore

pressure vent was not plugged during the test. Therefore, the pore pressure had not increased during the test, and permeability had diminished to zero.

The second brine permeability test was performed using Specimen CS/DC2/T2S-1/1 that had an initial fractional density of 0.86. The flow rates in this test were much higher than were observed in the first test, and the test was completed in about 1 hour. The flow versus time curve for the second test is shown in Figure 4-11, along with the calculated permeability value of 8.2×10^{-14} m^2.

The third and final brine permeability test was performed using the specimen identified as CS/DC1/8-3. The test conditions used were the same as those for the two previous brine permeability tests. The third brine permeability test had an initial fractional density of 0.86. The flow rates in this test were quite high and the accumulator used as a pressurized brine source held only about 4 liters of fluid. As a result, the accumulator was depleted in a short time, so three stages of the test were performed. Between stages, the confining pressure was reduced and the accumulator was refilled with brine. The confining pressure was then reapplied and the next stage of permeant flow was initiated. The data from the three stages were merged in chronological order and are shown in the flow versus time curve plotted in Figure 4-12. The data from the final two stages were used to calculate a permeability value of 1.5×10^{-14} m^2.

Five specimens prepared from the large-scale blocks were tested for permeability using nitrogen gas as the permeant fluid. Three of those specimens were tested at their initial fractional density (nominally 0.9) and two were mechanically deformed in a series of hydrostatic compaction/consolidation load paths so that the effect of density on permeability could be investigated. Although hydrostatic stresses of up to 15 MPa were used to increase the density of these two specimens, all permeability testing was performed at a hydrostatic stress of 1 MPa so that hydrostatic stress could be eliminated as a variable affecting the permeability measurements. Table 4-6 summarizes the permeability measurements recorded from these five specimens.

Specimen DCCS3/3/1-4 was mechanically deformed in its as-received state of moisture content; i.e., 0.44 percent. The stress and density history for this specimen is shown in Figure 4-13. For this specimen, the fractional density increased from 0.901 to 0.934 after approximately 21 days of testing and its permeability decreased from 5×10^{-14} m^2 to 5×10^{-15} m^2 over this range in fractional density.

The small change in fractional density exhibited by Specimen DCCS3/3/1-4 was attributed to the low moisture content of the specimen. Therefore, before starting the second test using Specimen DCCS3/2/2-1, the specimen was humidified to increase its moisture content to approximately the value specified in the large scale dynamic-compaction demonstration study (i.e., 1-percent). The

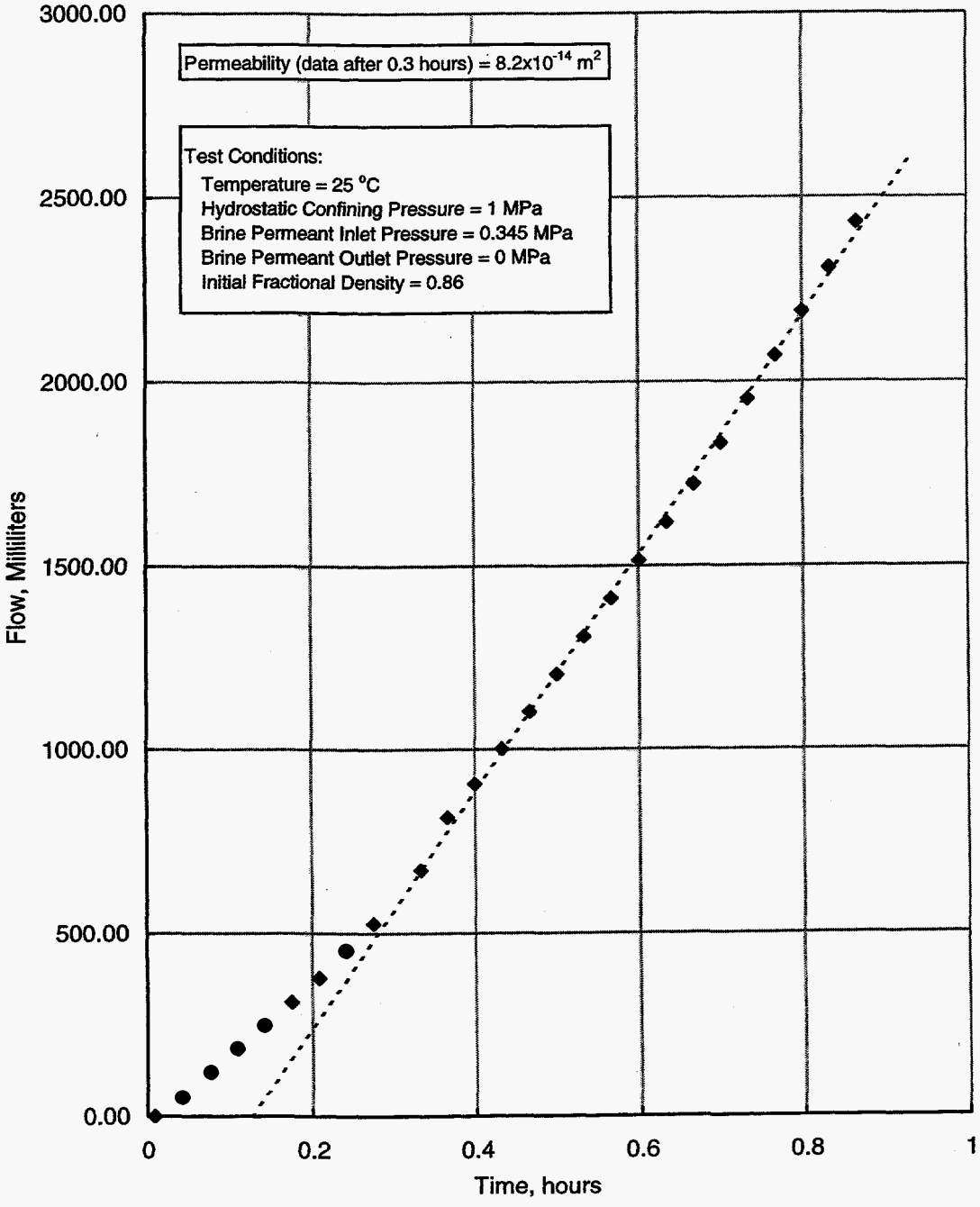

Figure 4-11. Permeability data for specimen CS/DC2/T2S-1/1.

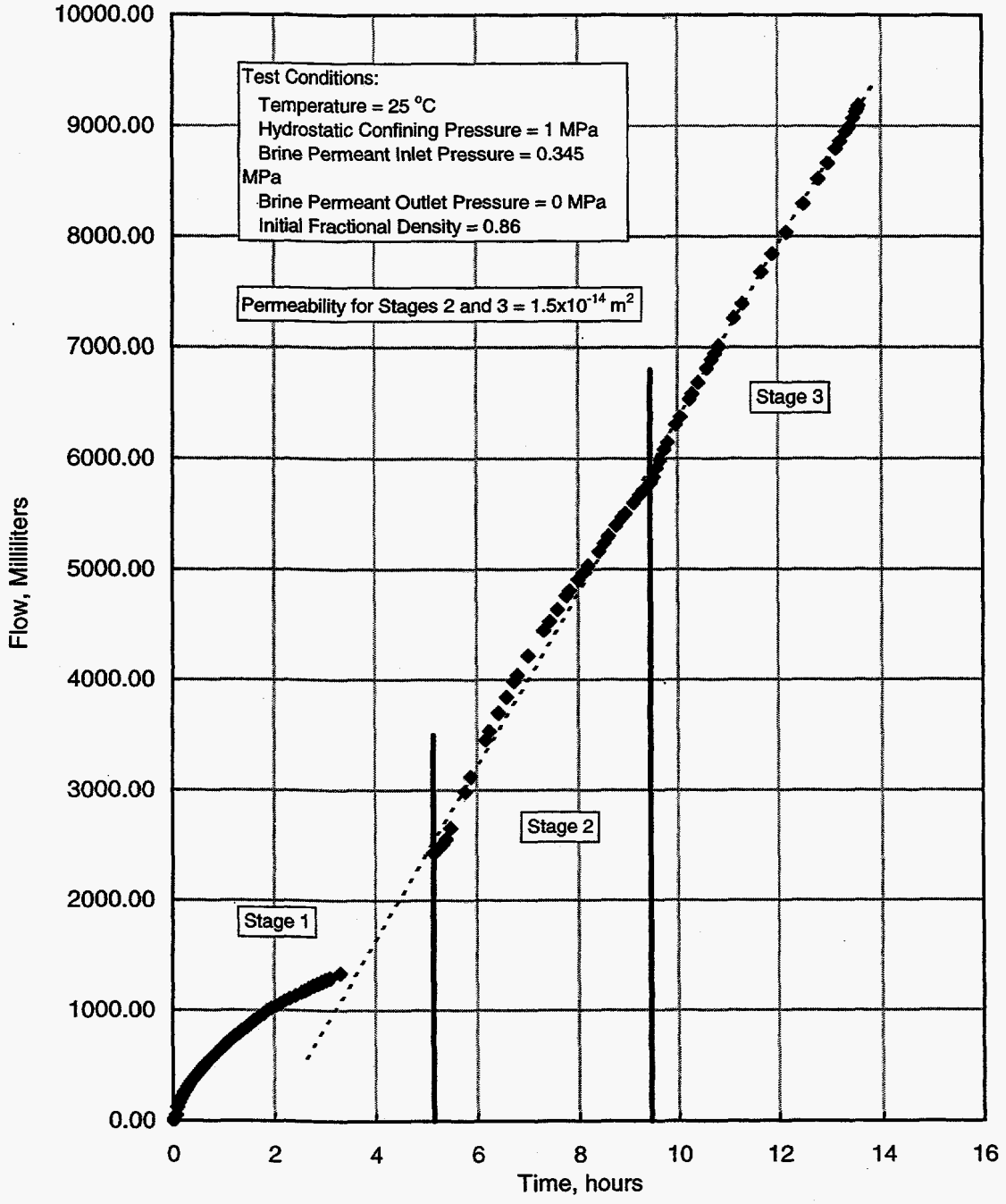

Figure 4-12. Permeability data for specimen CS/DC1/8-3.

Table 4-6. Summary of Gas Permeability Experiment

Specimen I.D.	Fractional Density	Permeability (m^2)
DCCS3/3/3-1	0.889	7.88×10^{-14}
DCCS3/2/1-1	0.901	4.99×10^{-14}
DCCS3/1/1-4	0.889	5.51×10^{-14}
DCCS3/3/1-4	0.901	4.99×10^{-14}
	0.916	2.63×10^{-14}
	0.929	4.58×10^{-15}
	0.934	4.95×10^{-15}
DCCS3/2/2-1	0.899	8.61×10^{-14}
	0.902	6.25×10^{-14}
	0.915	3.50×10^{-14}
	0.922	2.22×10^{-14}
	0.945	5.15×10^{-15}
	0.946	7.06×10^{-16}
	0.949	8.67×10^{-17}
	0.954	2.29×10^{-16}
	0.962	9.88×10^{-17}
	0.965	1.76×10^{-16}
	0.990	6.55×10^{-21}

moisture content of Specimen DCCS3/2/2-1 was 1.27 percent after humidification. Figure 4-14 provides the stress and density history for this specimen. As shown, the fractional density increased to about 0.97 within a time of approximately 3 hours. The rapid increase in density is attributed to the addition of the small amount of moisture. The permeability for this specimen changed from approximately 8.6×10^{-14} m^2 to 6.5×10^{-21} m^2. At the high fractional densities that occurred at the end of the test on Specimen DCCS3/2/2-1, the specimen is expected to have a high brine saturation because of the moisture added before the test began. Therefore, the low gas permeability measured at the end of the test probably represents a relative permeability value rather than the true intrinsic permeability and should be used with caution.

RSI-325-98-172

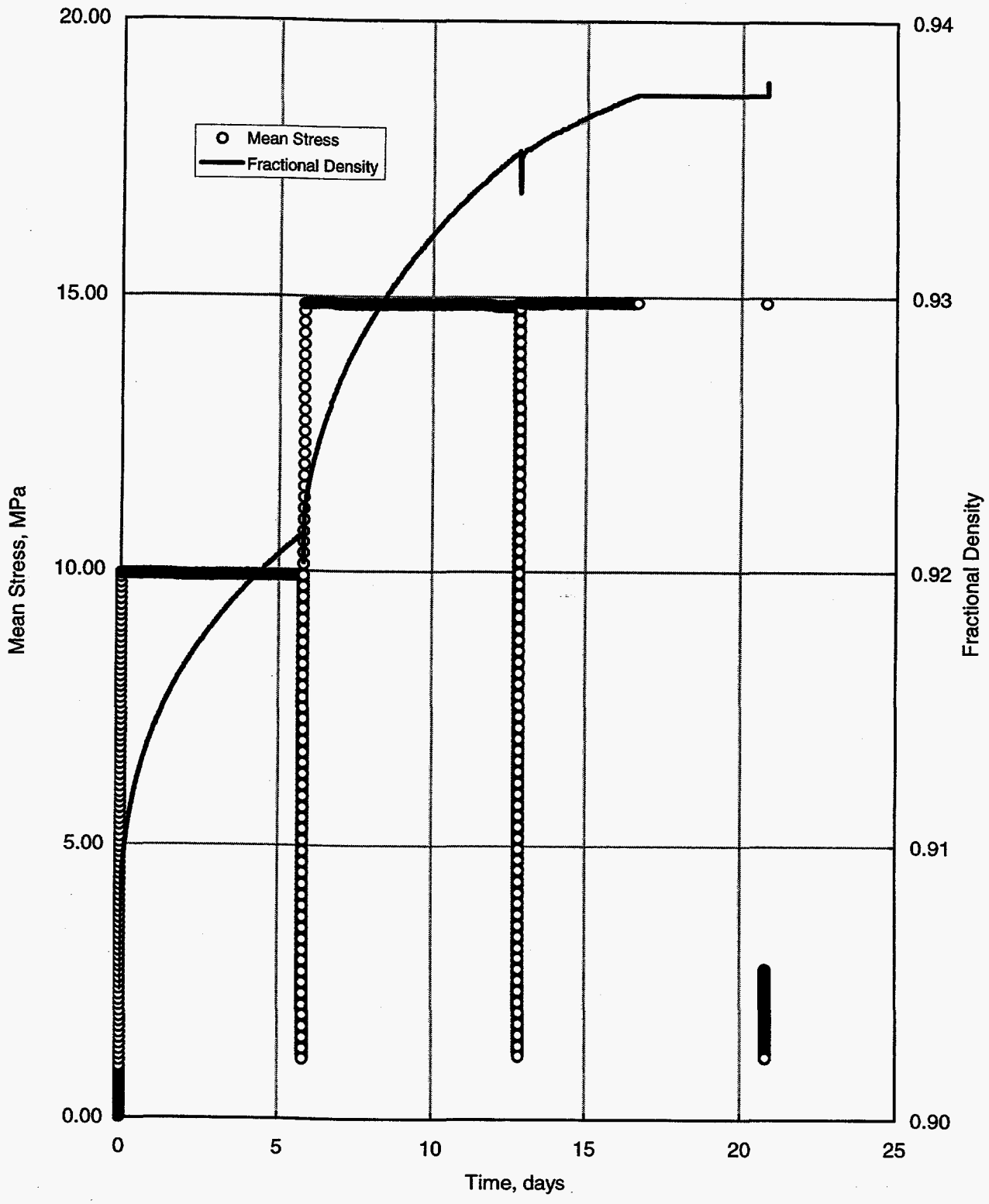

Figure 4-13. Stress and density history for permeability test on specimen DCCS3/3/1-4.

The permeability values from the three brine permeability tests (Table 4-5) and the five gas permeability tests (Table 4-6) were added to a previous database of laboratory permeability results (Appendix B) and field results generated for dynamically compacted crushed salt (Hansen and Ahrens, 1998). In compiling the combined database of permeability results, the values of fractional density reported in Appendix B were modified to account for differences in calculational methods. The fractional densities in Appendix B were calculated using the wet mass of the specimens and assuming the density of intact salt was 2.14 g/cc. The current calculations of fractional density use the dry mass of the specimen and a value of 2.16 g/cc for the density of intact salt. Thus, the fractional densities ($\overline{\rho}$) in Appendix B were corrected for water content, w, and higher density of intact salt using the expression:

$$\overline{\rho}_{2.16} = \frac{2.14}{2.16}\left(\frac{\overline{\rho}_{2.14}}{1+\frac{w}{100}}\right) \tag{4-13}$$

The moisture content for the two specimens listed as CS/DC1-4-1/3/1 and CS/DC1-8-3 in Appendix B was 0.26 percent. The moisture content for the other four specimens listed in Appendix B was 1.27 percent.

A significant difference among the permeability results was thought to be the difference in the type of permeant used. Some of the tests were performed using nitrogen gas as the permeant while the remainder of the tests used saturated brine as the permeant. The results from the two types of testing are compared in Figure 4-15, which plots permeability as a function of fractional density. As seen in the figure, the type of permeant used apparently has no major effect on the permeability determination, although the brine-based values do indicate a somewhat lower permeability than the permeability determined using gas. From only a few brine tests, statistically significant conclusions are not warranted. However, it is possible the effect results from salt precipitation at interstitial sites. A continuous decrease in brine permeability, while under constant conditions, was reported by Brodsky (1994).

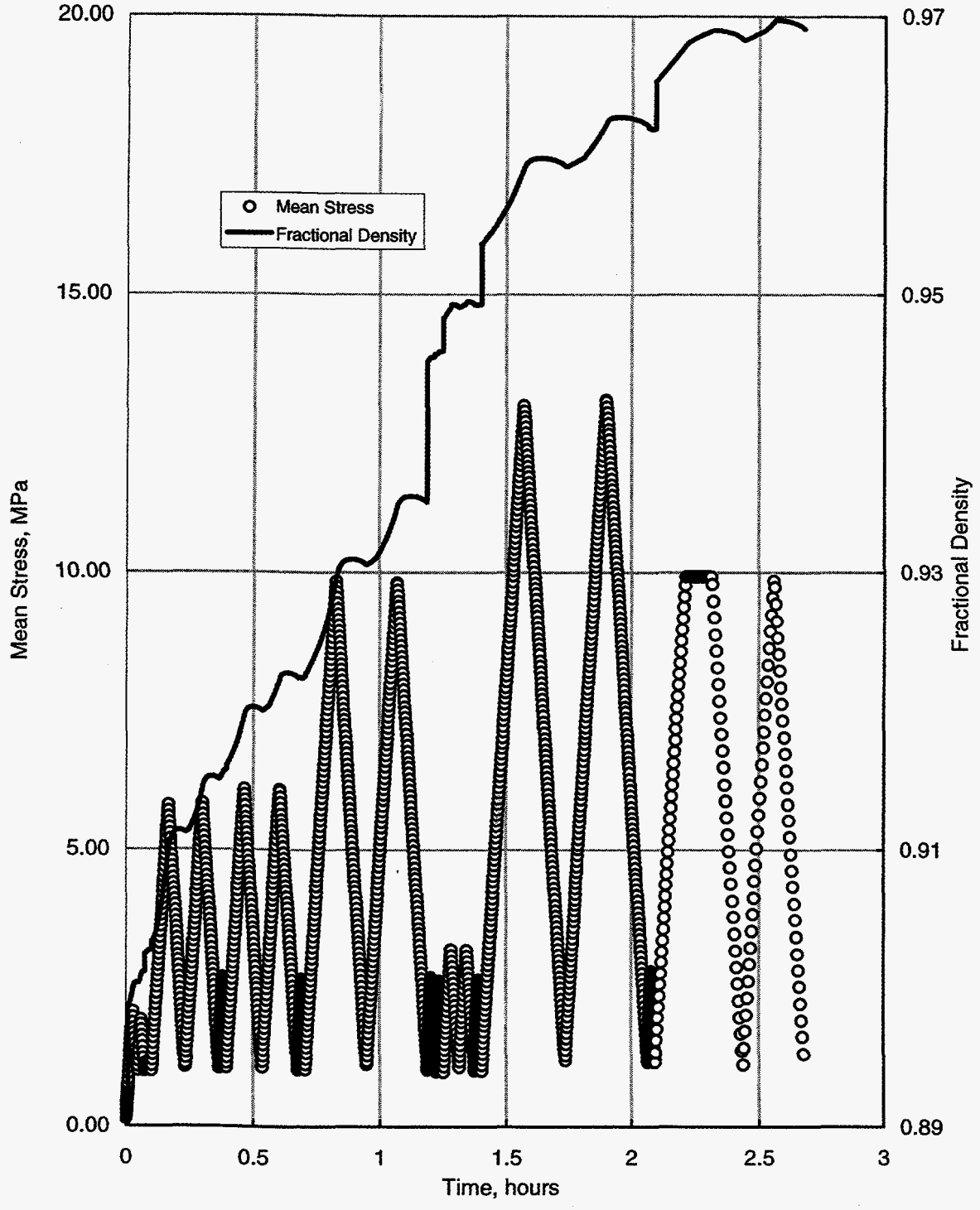

Figure 4-14. Stress and density history for permeability test on specimen DCCS3/2/2-1.

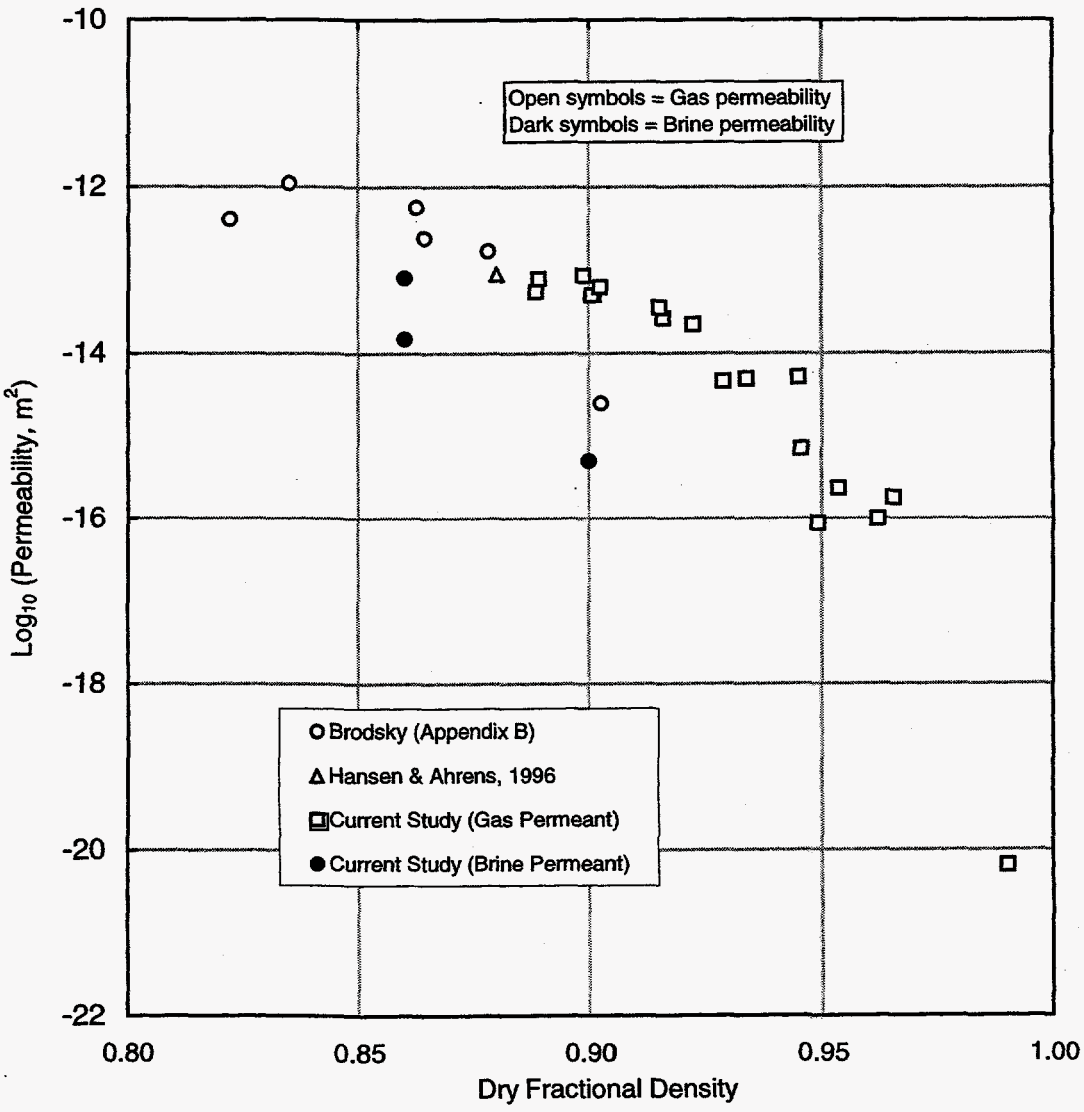

Figure 4-15. Permeability as a function of fractional density for dynamically compacted crushed salt.

Deformation data were collected from the gas permeability test on Specimen DCCS3/3/1-4 for estimating the bulk modulus, K, of the large-scale material. This provided additional information on a topic that has been investigated previously (Holcomb and Hannum, 1982); i.e., the dependence of the bulk modulus, K, on changes in fractional density. The results of the Holcomb and Hannum investigations, the test on the large-scale specimen, and the results tabulated in Table 4-3 are shown in Figure 4-16. Also shown on the figure is the value for intact salt (Munson et al., 1989). Even though the Holcomb and Hannum data were obtained using mine-run salt instead of dynamically compacted salt, the data clearly indicate that the bulk modulus of crushed salt increases nonlinearly toward the value for intact salt as the density increases. No current model was fit to describe this relationship, but a model fit by Holcomb and Hannum is shown on the figure and the current data appear to be in reasonable agreement with that model.

4.4 Substructures of Reconsolidated Crushed Salt

It has been postulated and confirmed that consolidation of granular rock salt occurs by two primary mechanisms: grain boundary pressure solution, and dislocation creep. Further, a minor amount of added moisture greatly enhances densification (Spiers and Brzesowsky, 1993). Consideration of the fundamental deformational processes guided formulation of the constitutive model for reconsolidating crushed salt (Callahan et al., 1998a). As crushed salt is loaded, the principal densification mechanism of fluid-phase grain boundary solution/redeposition is rampant. As consolidation proceeds, the material attains sufficient density that its response assumes the constitutive response of intact salt. Thus, the proper material law for reconsolidating crushed salt incorporates pressure solution and dislocation creep.

Photomicrographs of tamped and reconsolidated crushed salt, which display essential features, have been published by Brodsky et al. (1998). In this section, particular attention is given to microstructures of the reconsolidated laboratory-prepared specimens because of a unique phenomenon observed. Recall that laboratory-prepared specimens were fabricated in three lifts. Dynamic compaction, whether at the Proctor scale in the laboratory or at the full scale of construction, naturally creates more fine grain sizes at the surface than at depth in each lift. Scanning electron microscopy showed the grain size at the lift interfaces to be nearly the same as those created in the full-scale, dynamic-compaction construction demonstration (Hansen and Ahrens, 1998). Based on a considerable body of observational evidence, reconsolidation is governed by very effective pressure solution/redeposition processes occurring on the fine grains.

Figure 4-4 shows a complete cross-section of a consolidated three-lift specimen. After consolidation, the three-lift specimen actually bulged in a girdle at the lift interfaces. The reason for this behavior lies with the relatively finer grain size at the interface. The finer grain size (relative to the remainder of each lift) gives rise to more rapid grain boundary processes because

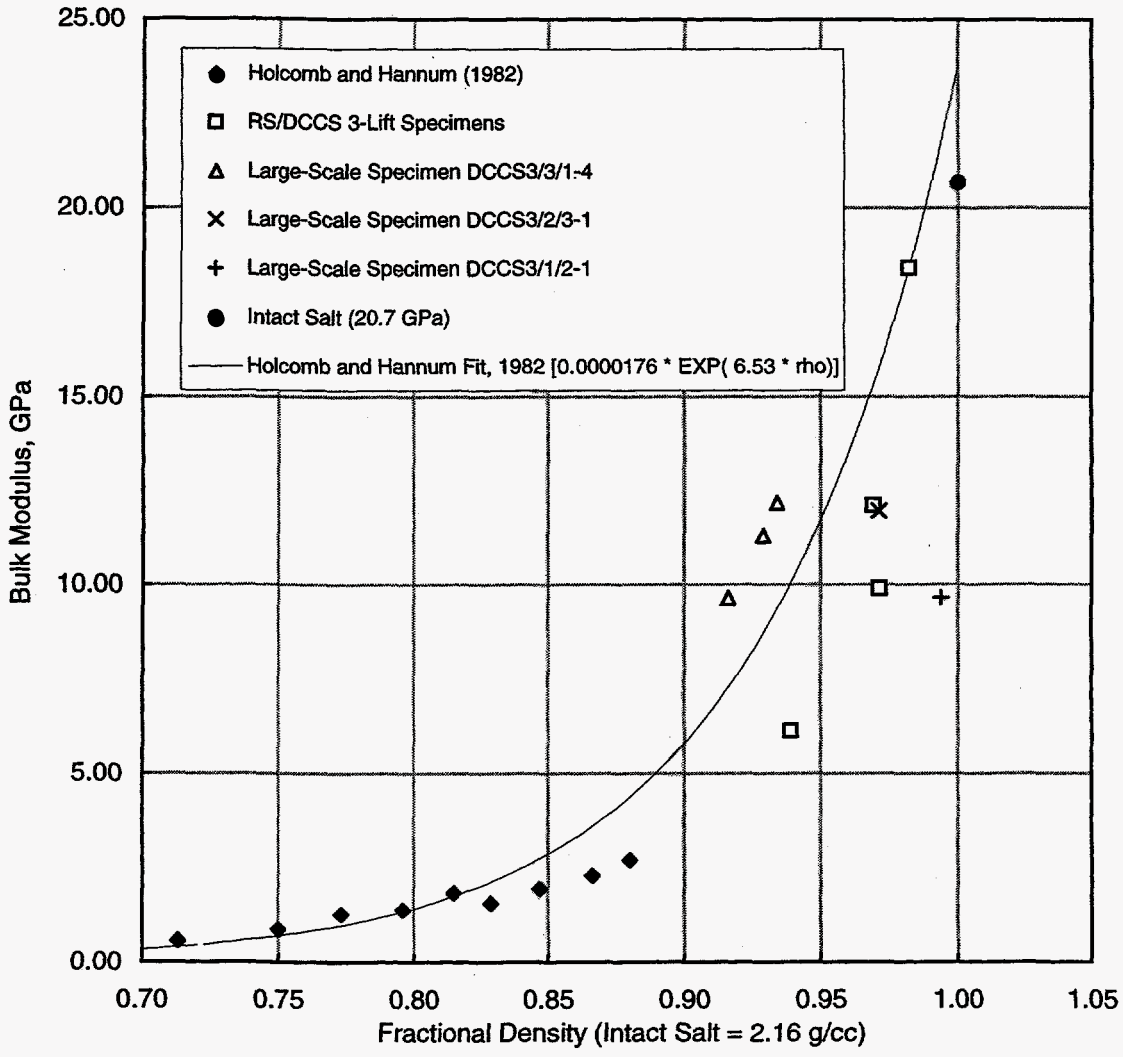

Figure 4-16. Bulk modulus as a function of fractional density.

of greater surface area available. The initial local density may also be higher than the initial average specimen density, which would also enhance the local change in consolidation mode. As the lift interface consolidates more rapidly than the rest of the specimen, the local density increases toward that of intact salt and the constitutive response changes from a consolidating mode to an intact mode. Hence, the bulges reflect locales where lateral deformation has reversed more readily from an inward direction (consolidation) to an outward direction, consistent with intact material response.

Two photomicrographs of the consolidation processes are provided in Figures 4-17 and 4-18. These examinations were made on the interface material. The first is an SEM micrograph shot at a magnification of 1,100. Note the grain size is approximately 20-30 um and almost no fine grains remain. Pressure solution is recognized by the triple junction of grains in the lower right field of view. The glossy nature of the surface is caused by cleavage fracture when the specimen surface was broken. No voids are evident, with an observation consistent with permeability diminishing to zero as consolidation approaches a fractional density of 0.95 and greater. The second is an optical micrograph with the scale bar shown on the figure. Healed grain boundaries can be discerned by the outline of fluid inclusions. Upon complete healing, these last inclusions will disappear and no optical evidence will remain of the former grain boundary. As grain boundaries heal, the very thin fluid films become isolated. These occluded fluid inclusions are displayed as the black, irregular spots in Figure 4-18. This optical photomicrograph shows the late stage of complete grain boundary healing.

RSI-325-98-177

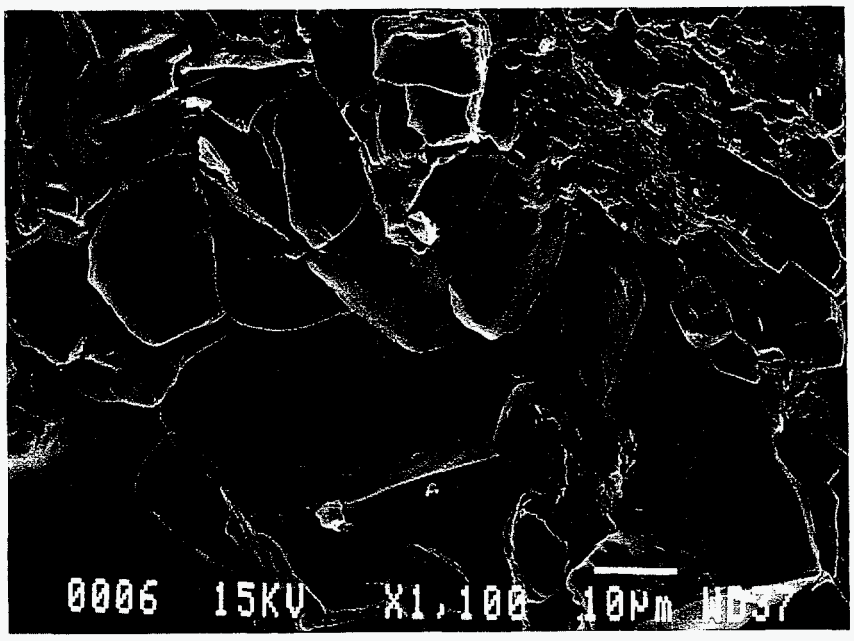

Figure 4-17. Reconsolidated three-lift sample on the fine-grained interface (SEM 1,100X).

RSI-325-98-176

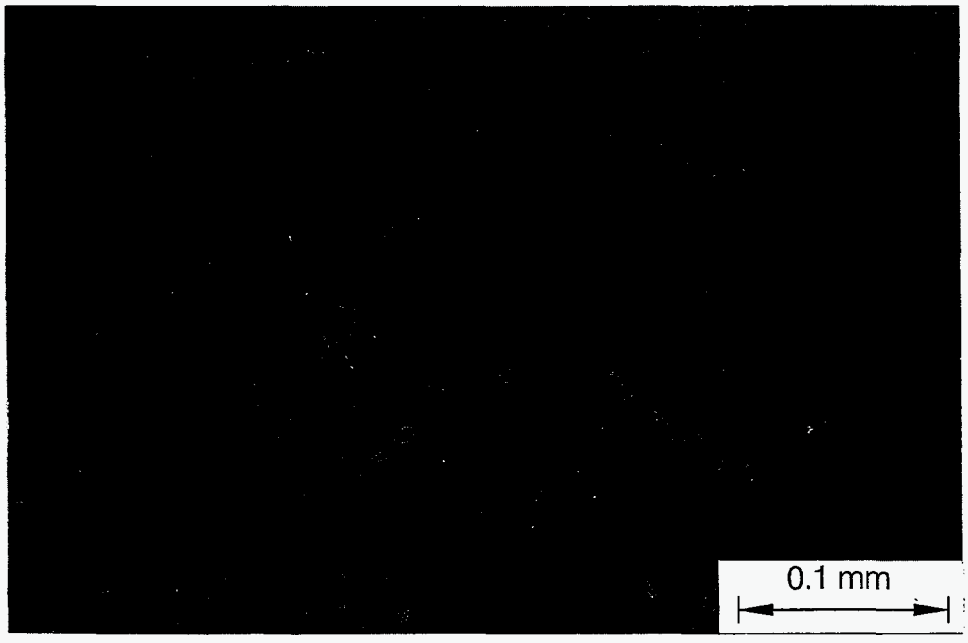

Figure 4-18. Healed grain boundaries of reconsolidating salt.

This page intentionally left blank

5.0 CONCLUSIONS

The work documented in this report demonstrated that dynamically compacted crushed-salt specimens could be fabricated on a laboratory scale using a relatively simple device. The dynamic-compaction procedure resulted in specimens that were very similar in fractional density (0.9), water content (1.6 percent), and fabric. The similarity among specimens helped reduce the specimen-to-specimen variability in the test results.

The permeability testing of the dynamically compacted crushed salt provided further evidence that the permeability decreases as the fractional density of the salt increases. This conclusion agrees with previous results. The current test results were added to the previous database of permeability results to reinforce that conclusion.

A suite of shear consolidation creep test results were added to a database of similar results for the purpose of estimating parameters in a constitutive model that represents the behavior of crushed salt (Callahan et al., 1998a). The current testing was performed at higher initial fractional densities (0.9) and stresses (1 to 5 MPa) than were used in previous programs to give better coverage of the range of conditions likely to be encountered during sealing operations at the WIPP. The current testing provided new observations on specimen deformation that confirmed constitutive model predictions. The constitutive model predicted that stress states existed where the radial strain rate would initially be positive (consolidation) and then reverse direction and become negative as the specimen density increased. This phenomenon was clearly observed in multiple tests.

Three constant axial strain-rate tests were performed. These three tests were not to be included in the database used for estimating the parameters in the constitutive model. The purpose of these tests was to provide results from a unique load path that could be used to evaluate the predictive capability of the constitutive model.

All of the observational microscopy supports the fundamental theory of densification behavior of wet granular salt. The constitutive model developed by Callahan and coworkers embodies the governing mechanisms as documented by the enclosed micrographs. The experimental behavior is found to be consistent with theory both in the mesoscopic scale of laboratory experiments as well as the microscopic scale where the processes occur. It is the complete understanding of reconsolidation processes, verified by laboratory experiments, parameterized in one database and predicted accurately in independent experiments, comprehensively embodied in the mathematical formulation of the constitutive equations that provide the scientific basis and confidence for performance predictions of compacted-salt seal performance.

This page intentionally left blank

6.0 REFERENCES

Brodsky, N.S. 1994. *Hydrostatic and Shear Consolidation Tests With Permeability Measurements on Waste Isolation Pilot Plant Crushed Salt.* SAND93-7058. Prepared by RE/SPEC Inc., Rapid City, SD. Albuquerque, NM: Sandia National Laboratories.

Brodsky, N.S., F.D. Hansen, and T.W. Pfeifle. 1998. "Properties of Dynamically Compacted WIPP Salt," *The Mechanical Behavior of Salt, Proceedings of the Fourth Conference, École Polytechnique de Montréal, Mineral Engineering Department, Québec, Canada, June 17-18, 1996.* SAND96-0838C. Eds. M. Aubertin and H.R. Hardy, Jr. Clausthal-Zellerfield, Germany: Trans Tech Publications. 303-316. (Copy on file in the Sandia WIPP Central Files, Sandia National Laboratories, Albuquerque, NM as WPO#49574.)

Callahan, G.D., K.D. Mellegard, and F.D. Hansen. 1998a. "Constitutive Behavior of Reconsolidating Crushed Salt," *Journal of Rock Mechanics and Mining Sciences.* SAND98-0179C, Paper No. 029. Vol. 35, no. 4-5, 422-423. (Paper presented at NARMS '98, 3rd North American Rock Mechanics Symposium, Cancún, Mexico, June 3-5, 1998. Paper No. 029 on CD-ROM distributed with journal.)

Callahan, G.D., M.C. Loken, L.D. Hurtado, and F.D. Hansen. 1998b. "Evaluation of Constitutive Models for Crushed Salt," *The Mechanical Behavior of Salt, Proceedings of the Fourth Conference, École Polytechnique de Montréal, Mineral Engineering Department, Québec, Canada, June 17-18, 1996.* SAND96-0791C. Eds. M. Aubertin and H.R. Hardy, Jr. Clausthal-Zellerfield, Germany: Trans Tech Publications. 317-330. (Copy on file in the Sandia WIPP Central Files, Sandia National Laboratories, Albuquerque, NM as WPO#49573.)

Hansen, F.D. 1997. "Reconsolidating Salt: Compaction, Constitutive Modeling and Physical Processes," *International Journal of Rock Mechanics & Mining Sciences.* SAND97-0484C, Paper No. 119. Vol. 34, no. 3-4, 492. (Paper presented at NYRocks'97, 36th Rock Mechanics Symposium, New York, NY, June 29-July 2, 1997. Paper No. 119 on CD-ROM distributed with journal.)

Hansen, F.D., and E.H. Ahrens. 1998. "Large-Scale Dynamic Compaction of Natural Salt," The Mechanical Behavior of Salt, Proceedings of the Fourth Conference, École Polytechnique de Montréal, Mineral Engineering Department, Québec, Canada, June 17-18, 1996. SAND96-0792C. Eds. M. Aubertin and H.R. Hardy, Jr. Clausthal-Zellerfield: Trans Tech Publications. 353-364. (Copy on file in the Sandia WIPP Central Files, Sandia National Laboratories, Albuquerque, NM as WPO#49640.)

Holcomb, D.J., and D.W. Hannum. 1982. *Consolidation of Crushed Salt Backfill Under Conditions Appropriate to the WIPP Facility.* SAND82-0630. Albuquerque, NM: Sandia National Laboratories.

Mellegard, K.D., T.W. Pfeifle, A.F. Fossum, and P.E. Senseny. 1993. "Pressure and Flexible Membrane Effects on Direct-Contact Extensometer Measurements in Axisymmetric Compression Tests," *Journal of Testing and Evaluation.* Vol. 21, no. 6, 530-538.

Munson, D.E., A.F. Fossum, and P.E. Senseny. 1989. *Advances in Resolution of Discrepancies Between Predicted and Measured In Situ WIPP Room Closures.* SAND88-2948. Prepared by RE/SPEC Inc., Rapid City, SD. Albuquerque, NM: Sandia National Laboratories.

Sandia National Laboratories. 1996. *Waste Isolation Pilot Plant Shaft Sealing System Compliance Submittal Design Report, Volume 1 of 2: Main Report. Appendices A, B, C, and D.* SAND96-1326/1. Albuquerque, NM: Sandia National Laboratories.

Spiers, C.J., and R.H. Brzesowsky. 1993. "Densification Behavior of Wet Granular Salt: Theory Versus Experiment," *Seventh Symposium on Salt, Kyoto, Japan, April 6-9, 1992.* Eds. H. Kakihana, H.R. Hardy, Jr., T. Hoshi, and K. Toyokura. Amsterdam; New York, New York: Elsevier Science Publishers B.V. Vol. I, 83-92. (Copy on file in the Sandia WIPP Central Files, Sandia National Laboratories, Albuquerque, NM as WPO#39215.)

APPENDIX A
MEMORANDUM TO L.D. HURTADO
RE: OBSERVATIONS AND RECOMMENDATIONS REGARDING DYNAMICALLY COMPACTED SAMPLES

Sandia National Laboratories

Operated for the U.S. Department of Energy by
Sandia Corporation
P.O. Box 5800
Albuquerque, NM 87185-1395

Frank D. Hansen
WIPP Technical Integration Dept. Org. 6801

Mailing Address: 115 N. Main St., Carlsbad, NM 88220
Phone: (505) 234-0066 (Carlsbad)
Fax: (505) 234-0061
Internet: fdhanse@sandia.gov

November 17, 1997

L. D. Hurtado MS 1322
Sandia National Laboratories
P. O. Box 5800
Albuquerque, NM 87185

Subject: Observations and recommendations regarding dynamically compacted samples

Dear L. D.:

Introduction

On Friday November 14 I examined a compacted sample of WIPP crushed salt that had been prepared by RE/SPEC, Inc. The Scanning Electron Microscope at SDSM&T, Rapid City SD was used, as in previous observations discussed here. Because of its depth of field and very high magnification, SEM is used to characterize the minute fabric on surfaces of compacted crushed salt samples. The fabric comprising size, shape and arrangement of grains is important to reconsolidation processes. Because large-scale dynamic compaction is the specified construction technique for placing crushed salt in WIPP shafts, laboratory samples prepared for experiments should closely match the fabric of that produced by large-scale dynamic compaction. At this point, only 4 samples remain from the large-scale demonstration itself. The microscopic study summarized in this letter is primarily to assess how closely lab-prepared compaction samples match those created by large-scale dynamic compaction.

This letter characterizes the original fabric of three dynamically compacted samples. The original fabric is that which is created by the dynamic compaction process, before any further consolidation is imparted by laboratory experiments. The three compacted samples include one from the large-scale dynamic compaction demonstration, one from a well compacted 3-lift lab sample, and one from a new 10-lift lab sample, prepared by reduction of drop height. A fourth photograph shows the consolidated fabric of the fine-grained interface of the 3-lift sample. Multiple photomicrographs were shot of several distinct surfaces representing these three preparation techniques, but only one photomicrograph of each is shown here.

Descriptions of Substructures

Large-Scale Dynamic Compaction. (Photograph #0003). A heterogeneous gradation of fine particulate is seen . Grain boundaries are open. Grains produced during the large-scale dynamic compaction demonstration are abraded and rounded, rather than cleaved. Rounded, abraded larger (20-30 μm) grains and a significant population of fine grains (<10 μm) as seen in Photograph #0003 indicate physical abrasion occurs in large-scale dynamic compaction.

Three-Lift Lab-Prepared Sample. (Photograph #0001). Relatively uniformly sized (20-30 μm) cubic cleaved crystals comprise the ground mass. Grain boundaries are tighter than those produced by large-scale dynamic compaction, as can be seen by comparison to Photograph #0003. The density represented by the 3-lift sample is similar to that of the large-scale dynamically compacted sample, but the cubic cleaved grains indicate less abrasion than experienced by the large-scale sample. Fewer fine grains possessing diameters less than 10 μm are present in the 3-lift sample than found in the large-scale dynamic compaction sample.

Ten-Lift Lab-Prepared Sample. (Photograph #0014). Greater void space is apparent here than in the other two samples. Cubic shape is consistent with the 3-lift sample, indicating less abrasion for both lab techniques than experienced in large dynamic compaction. Fine grain size is about 10 μm, with "larger" grains about 20-30 μm (microns). More 10 μm grains are present and bonded, which perhaps results from the addition of 2 wt % water. Grains appear slightly "washed".

Three-Lift After Reconsolidation. (Photograph #0006). This particular photograph is taken from the "bulged" zone. That is, consolidation of the three lift sample was nonuniform and accentuated at the lift interface where grain size was visibly finer than the remainder of the sample volume. As can be seen, the grain size at the bulged interface is uniformly 20 μm. This is evidence that grain size of the original 3-lift sample as shown in Photograph #0001 is preserved. The microprocess of pressure solution/redeposition operates effectively on points of stress concentration, filling interstitial voids rapidly without greatly changing the original grain diameter. In addition, the consolidated fabric shown in Photograph #0006 is indistinguishable from the consolidated large-scale dynamic compaction substructure. The size and density of grains occupying the 3-lift interfaces are quite representative of the large scale dynamic compaction sample.

Discussion and Recommendations.

I recommend using the 3-lift, well compacted lab-prepared samples for further testing.

Reasons for this conclusion include the following:

1. The grain size in the fine grained interface zone is very similar to that of large-scale dynamic compaction. (about 20 μm), although the 3-lift sample lacks a population of grains from 1-3 μm.
2. Density of the 3-lift lab-prepared sample equals that of the large-scale dynamic compaction.
3. Consolidated substructures for the 3-lift samples and consolidated substructures of the large-scale dynamic compaction samples are similar (20 μm).

The bulged zones in the 3-lift samples represent accentuated deformation relative to the remainder of the sample. It was felt that the evident finer grains at the lift interface may influence results and representativeness of these experiments. Based on SEM observations, it appears that interface fines on the 3-lift samples are a close approximation to the large-scale dynamic samples because the density is the same and the grain size similar, although lacking some of the finer distributions.

Care should be exercised during addition of water to the 3-lift samples. Based on SEM observations, it appears that the lab samples, particularly the 10-lift sample, contain more water than the large-scale dynamically compacted sample. That is, the grains in the 10-lift sample are "washed" by the moisture. The water content should be monitored to be about 1.5 wt %.

If you have any problem interpreting these conclusions, please call me at 505-234-0066.

Sincerely,

F. D. Hansen

Copy to:
Mr. T. W. Pfeifle, RE/SPEC

SNL:
MS 1322 F. D. Hansen
MS 1322 D. S. Coffey
SWCF-C:1.1.03.2.1: DPRP1:SE:DES:QA:AG-4911,RE/SPEC, Task 17

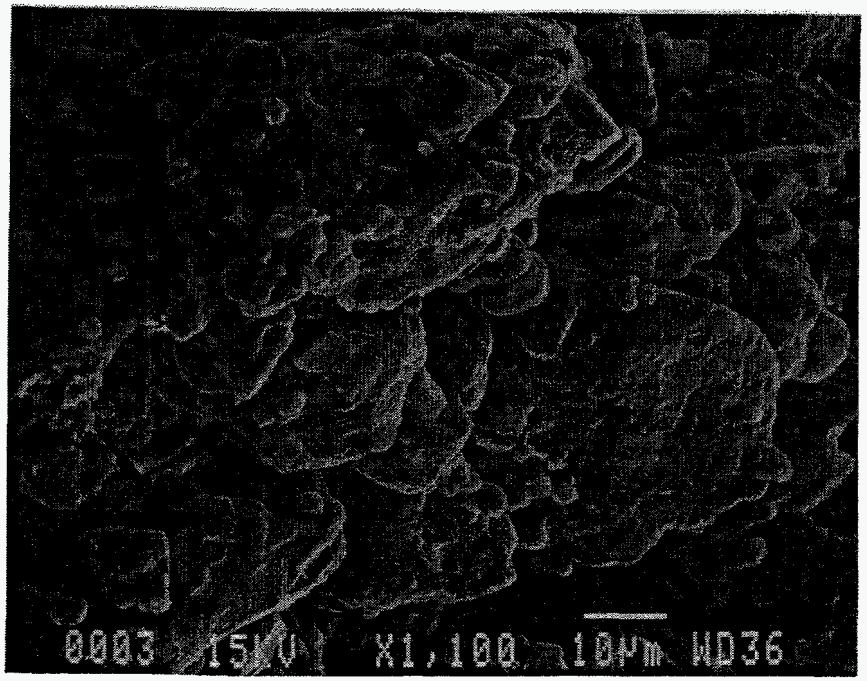

Figure A-1. Photograph #0003: Original fabric of large-scale dynamically compacted crushed salt.

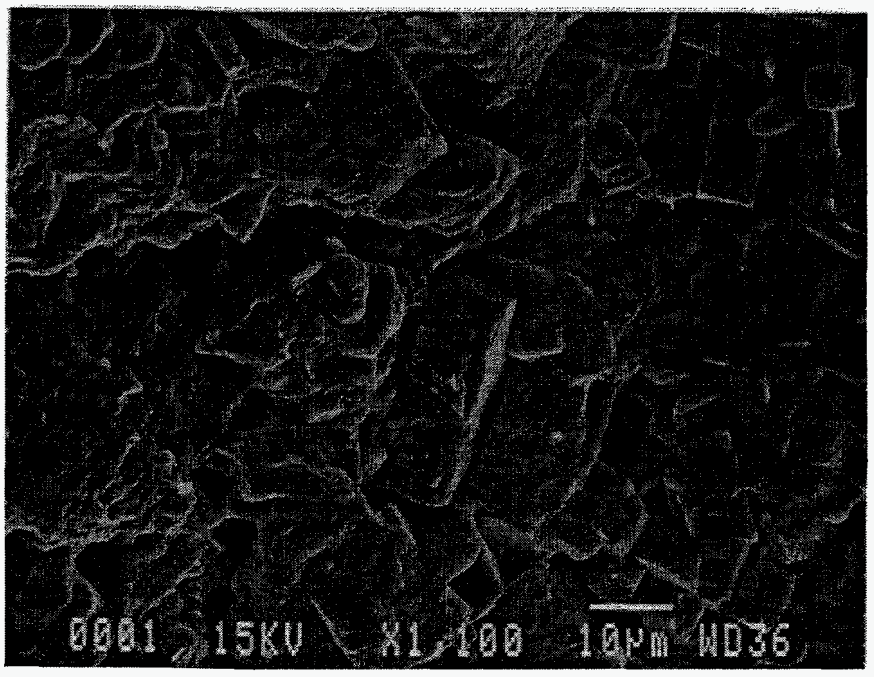

Figure A-2. Photograph #0001: Original fabric of three-lift, laboratory-prepared sample of crushed salt.

Figure A-3. Photograph #0014: Original fabric of ten-lift laboratory-prepared sample of crushed salt.

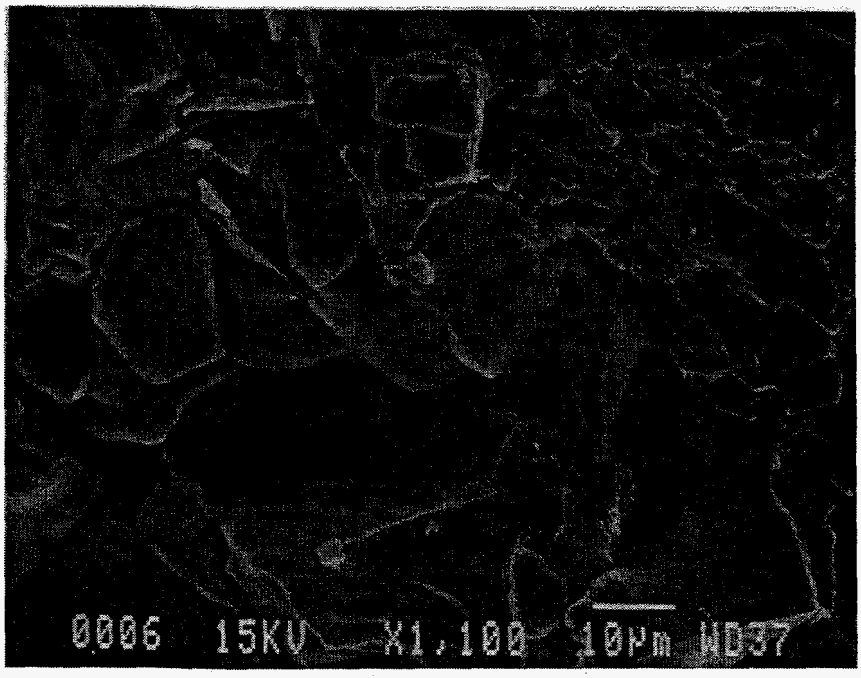

Figure A-4. Photograph #0006: Reconsolated three-lift sample on the fine grained interface.

APPENDIX B
MEMORANDUM TO F.D. HANSEN RE: PROGRESS REPORT FOR SANDIA NATIONAL LABORATORIES CONTRACT AA-2020 COVERING THE PERIOD SEPTEMBER 1, 1994 TO SEPTEMBER 30, 1994

RE/SPEC INC.
RESEARCH/SPECIALISTS

Rapid City, South Dakota • Albuquerque, New Mexico
Pierre, South Dakota • Minneapolis, Minnesota

External Memorandum

To: Sandia National Laboratories
Attn: Dr. Frank D. Hansen (6121)
P.O. Box 5800
Albuquerque, NM 87185-5800

cc: Mr. Gary Romero (10233)
Dr. Arlo F. Fossum (RE/SPEC Inc.)
Mr. Darrell K. Svalstad (RE/SPEC Inc.)
Mr. Tom W. Pfeifle (RE/SPEC Inc.)
Mr. Leo Van Sambeek (RE/SPEC Inc.)
Laboratory Staff
248C GR6.1

From: Dr. Nancy S. Brodsky NSB
RE/SPEC Inc.
P.O. Box 725
Rapid City, SD 57709

Date: October 12, 1994

Subject: Progress Report for Sandia National Laboratories Contract AA-2020 Covering the Period September 1, 1994 to September 30, 1994.

Project Administration and QA. Routine administrative and quality assurance activities were performed.

Permeability Tests. The previous progress report suggested that we had reached the upper detection limit for the manometer system that was used for gas permeability measurements. The gas flow rates measured for Specimens CS/DC1-4-1/3/1 and CS/DC2MM-2/1 were both near the maximum flow rate limit. Although the equivalent liquid permeability as determined using a Klinkenberg correction was reasonable for Specimen CS/DC1-4-1/3/1 (2.5×10^{-15} m^2), a negative value was obtained for Specimen CS/DC2MM-2/1. (The Klinkenberg correction is determined by performing a straight line fit to the permeability-versus-inverse mean gas pressure data. The permeability value determined at an inverse mean pressure of zero, i.e., at infinite pressure, is the equivalent liquid permeability or Klinkenberg-corrected permeability. The equivalent liquid permeability should be less than the gas permeability.)

The test system was reconfigured as described in the previous progress report and gas permeability measurements were made using flow meters. The system was checked for gas leaks using "Snoop," a commercially available clear liquid that is placed on all of the connection points to detect gas bubbles. A Klinkenberg correction could not be applied to these measurements because only a single value of gas inflow pressure could be used.

The gas permeabilities measured to date on dynamically compacted crushed salt are summarized in Table 1. Unfortunately, Specimen CS/DC1-4-1/3/1 had been epoxy-impregnated and sectioned and so its permeability could not be remeasured using the flow meter system. The permeability data are plotted in Figure 1 along with data given in Brodsky [1993][1]. There is no systematic difference between the permeabilities measured for the two different sample shipments even though they differed in moisture content (CS/DC2 specimens had 1 percent moisture added whereas CS/DC1 specimens did not). Based on relative permeability effects, the permeabilities of CS/DC2 specimens were expected to be lower than in CS/DC1 specimens. The gas permeabilities are above the projection of the straight-line fit to the brine permeability data by about 2 orders of magnitude. Barring relative permeability effects, one would expect gas permeabilities to be higher than brine permeabilities because of the Klinkenberg effect; however, for Specimen CS/DC1-4-1/3/1, the Klinkenberg correction changed the permeability value by less than a factor of 2.

Table 1. Summary of Permeability Measurements on Dynamically Compacted Crushed Salt Specimens

Specimen ID[(a)]	Fractional Density [(b)]	Permeability (m^2)	Measurement Method
CS/DC1-8-3	0.875	2.43×10^{-13}	Flowmeter
CS/DC1-4-1/3/1	0.913	2.50×10^{-15}	Manometer; Klinkenberg-corrected value
CS/DC2/MM-1/1	0.898	1.71×10^{-13}	Flowmeter
CS/DC2/MM-2/1	0.840	4.11×10^{-13}	Flowmeter
CS/DC2/T2S-1/1	0.882	5.71×10^{-13}	Flowmeter
CS/DC2/T2S-3/2	0.853	1.10×10^{-12}	Flowmeter

(a) CS = Crushed Salt; DC1 = Dynamically Compacted, First Shipment; DC2 = Dynamically Compacted, Second Shipment.

(b) Fractional density is based on an intact density of 2140 $kg \cdot m^{-3}$ and the specimen volume determined before permeability testing was initiated. The permeability tests were conducted at 1 MPa confining pressure and in some cases additional consolidation occurred during the test.

[1]**Brodsky, N. S., 1993.** *Hydrostatic and Shear Consolidation Tests With Permeability Measurements on Waste Isolation Pilot Plant Crushed Salt*, SAND93-7058, prepared by RE/SPEC Inc, Rapid City, SD, for Sandia National Laboratories, Albuquerque, NM.

As an additional check on the testing method, a steel specimen was placed in the pressure vessel after testing was completed and a "permeability test" was run. As expected, there was no detectable gas flow. While this does not ensure that there were no leaks in the system during testing that would have caused erroneously high permeability values, it does lend some reassurance.

Projected Activities for the Next Reporting Period. The Sandia Technical Representative (Dr. Frank Hansen) is planning to visit the RE/SPEC Rapid City facility during the next reporting period. The status of this work and future direction will be discussed at that time.

NSB:sdc

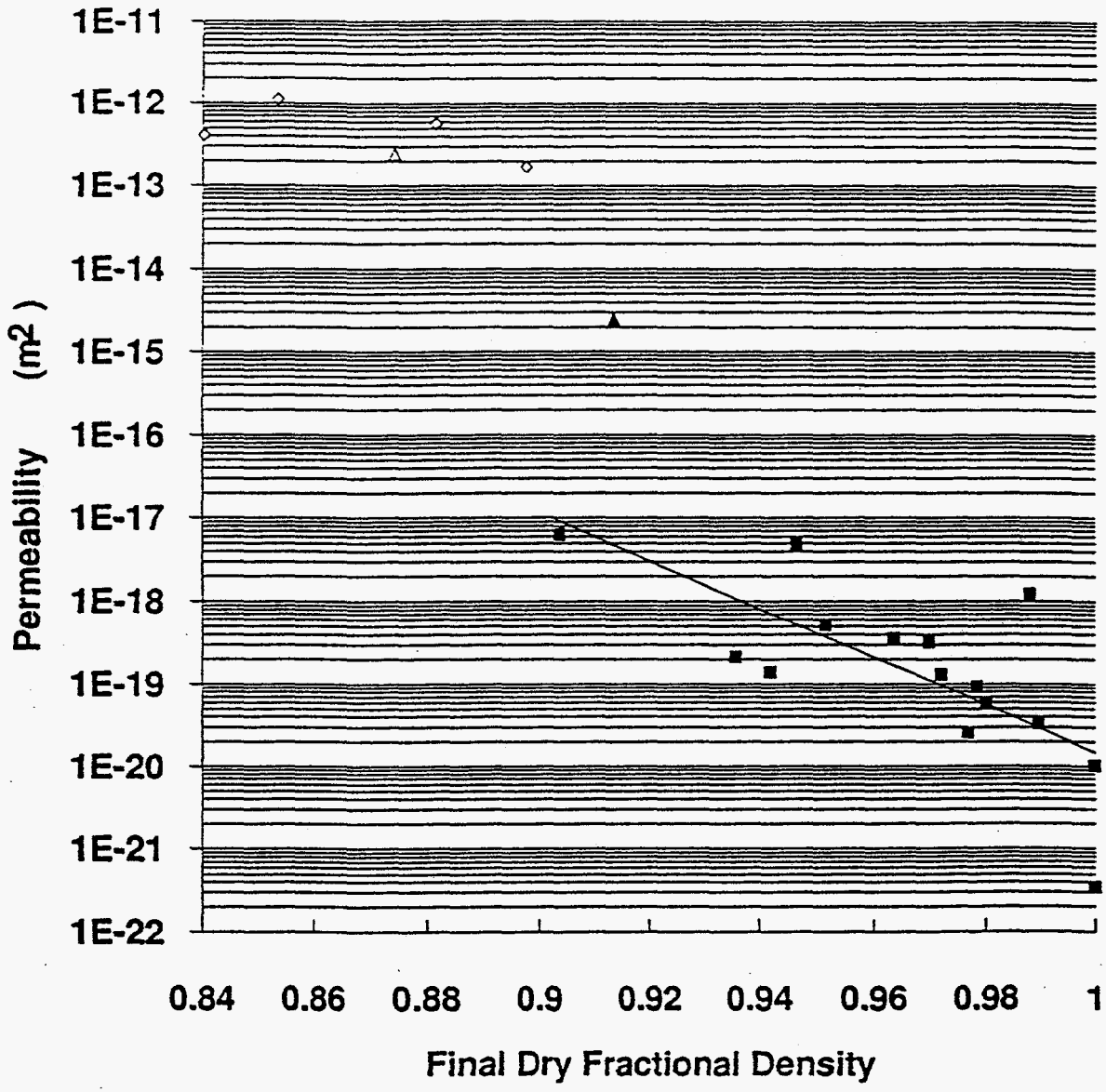

Figure 1. Permeability-versus-fractional density for crushed salt specimens. Solid squares represent brine permeability measurements given in Brodsky [1993] and a linear fit to that data is given. Triangles represent CS/DC1 specimens and diamonds represent CS/DC2 specimens. Unfilled symbols (diamonds and one triangle) indicate use of a flow meter and the solid triangle indicates use of a manometer and the application of a Klinkenberg correction.

This page intentionally left blank

WIPP
UC721 - DISTRIBUTION LIST
SAND98-2046

Federal Agencies

US Department of Energy (4)
Office of Civilian Radioactive Waste Mgmt.
Attn: Deputy Director, RW-2
Acting Director, RW-10
Office of Human Resources & Admin.
Director, RW-30
Office of Program Mgmt. & Integ.
Director, RW-40
Office of Waste Accept., Stor., & Tran.
Forrestal Building
Washington, DC 20585

Yucca Mountain Site Characterization Office
Director, RW-3
Office of Quality Assurance
Attn: Project Director
P. O. Box 30307
Las Vegas, NV 89036-0307

US Department of Energy
Research & Waste Management Division
Attn: Director
P.O. Box E
Oak Ridge, TN 37831

US Department of Energy (5)
Carlsbad Area Office
Attn: G. T. Basabilvazo
D. Galbraith
M. McFadden
R. Lark
J. A. Mewhinney
P.O. Box 3090
Carlsbad, NM 88221-3090

US Department of Energy
Office of Environmental Restoration and
Waste Management
Attn: M. Frei, EM-30
Forrestal Building
Washington, DC 20585-0002

US Department of Energy (3)
Office of Environmental Restoration and
Waste Management
Attn: J. Juri, EM-34, Trevion II
Washington, DC 20585-0002

US Department of Energy
Office of Environmental Restoration and
Waste Management
Attn: S. Schneider, EM-342, Trevion II
Washington, DC 20585-0002

US Department of Energy (2)
Office of Environment, Safety & Health
Attn: C. Borgstrom, EH-25
R. Pelletier, EH-231
Washington, DC 20585

US Department of Energy (2)
Idaho Operations Office
Fuel Processing & Waste Mgmt. Division
785 DOE Place
Idaho Falls, ID 83402

US Environmental Protection Agency (2)
Radiation Protection Programs
Attn: M. Oge
ANR-460
Washington, DC 20460

Boards

Defense Nuclear Facilities Safety Board
Attn: D. Winters
625 Indiana Ave. NW, Suite 700
Washington, DC 20004

Nuclear Waste Technical Review Board (2)
Attn: Chairman
J. L. Cohon
2300 Clarendon Blvd. Ste 1300
Arlington, VA 22201-3367

State Agencies

Attorney General of New Mexico
P.O. Drawer 1508
Santa Fe, NM 87504-1508

Environmental Evaluation Group (3)
Attn: Library
7007 Wyoming NE
Suite F-2
Albuquerque, NM 87109

NM Environment Department (3)
Secretary of the Environment
1190 St. Francis Drive
Santa Fe, NM 87503-0968

NM Bureau of Mines & Mineral Resources
Socorro, NM 87801

Laboratories/Corporations

Battelle Pacific Northwest Laboratories
Battelle Blvd.
Richland, WA 99352

Los Alamos National Laboratory
Attn: B. Erdal, INC-12
P.O. Box 1663
Los Alamos, NM 87544

Tech Reps, Inc. (3)
Attn: J. Chapman (1)
Loretta Robledo (2)
5000 Marble NE, Suite 222
Albuquerque, NM 87110

Westinghouse Electric Corporation (5)
Attn: Library
J. Epstein
J. Lee
R. Kehrman
P.O. Box 2078
Carlsbad, NM 88221

S. Cohen & Associates
Attn: Bill Thurber
1355 Beverly Road
McLean, VA 22101

RE/SPEC Inc. (2)
Attn: K.D. Mellegard
T. W. Pfeifle
P. O. Box 725
Rapid City, SD 57709-0725

National Academy of Sciences
WIPP Panel

Tom Kiess (15)
Staff Study Director
GF456
2101 Constitution Ave.
Washington, DC 20418

Universities

University of New Mexico
Geology Department
Attn: Library
141 Northrop Hall
Albuquerque, NM 87131

University of Washington
College of Ocean & Fishery Sciences
Attn: G. R. Heath
583 Henderson Hall, HN-15
Seattle, WA 98195

Libraries

Thomas Brannigan Library
Attn: D. Dresp
106 W. Hadley St.
Las Cruces, NM 88001

Government Publications Department
Zimmerman Library
University of New Mexico
Albuquerque, NM 87131

New Mexico Junior College
Pannell Library
Attn: R. Hill
Lovington Highway
Hobbs, NM 88240

New Mexico State Library
Attn: N. McCallan
325 Don Gaspar
Santa Fe, NM 87503

New Mexico Tech
Martin Speere Memorial Library
Campus Street
Socorro, NM 87810

WIPP Public Reading Room
Carlsbad Public Library
101 S. Halagueno St.
Carlsbad, NM 88220

Foreign Addresses

Atomic Energy of Canada, Ltd.
Whiteshell Laboratories
Attn: B. Goodwin
Pinawa, Manitoba, CANADA R0E 1L0

Francois Chenevier (2)
ANDRA
Parc de la Croix Blanche
1-7 rue Jean Monnet
92298 Chatenay-Malabry Cedex
FRANCE

Claude Sombret
Centre d'Etudes Nucleaires de la Vallee Rhone
CEN/VALRHO
S.D.H.A. B.P. 171
30205 Bagnols-Sur-Ceze
FRANCE

Commissariat a L'Energie Atomique
Attn: D. Alexandre
Centre d'Etudes de Cadarache
13108 Saint Paul Lez Durance Cedex
FRANCE

Bundesanstalt fur Geowissenschaften und
Rohstoffe
Attn: M. Langer
Postfach 510 153
D-30631 Hannover
GERMANY

Bundesministerium fur Forschung und
Technologie
Postfach 200 706
5300 Bonn 2
GERMANY

Institut fur Tieflagerung
Attn: K. Kuhn
Theodor-Heuss-Strasse 4
D-3300 Braunschweig
GERMANY

Gesellschaft fur Anlagen und Reaktorsicherheit
(GRS)
Attn: B. Baltes
Schwertnergasse 1
D-50667 Cologne
GERMANY

Shingo Tashiro
Japan Atomic Energy Research Institute
Tokai-Mura, Ibaraki-Ken, 319-11
JAPAN

Netherlands Energy Research Foundation ECN
Attn: J. Prij
3 Westerduinweg
P.O. Box 1
1755 ZG Petten
THE NETHERLANDS

Svensk Karnbransleforsorjning AB
Attn: F. Karlsson
Project KBS (Karnbranslesakerhet)
Box 5864
S-102 48 Stockholm
SWEDEN

Nationale Genossenschaft fur die Lagerung
Radioaktiver Abfalle (2)
Attn: S. Vomvoris
P. Zuidema
Hardstrasse 73
CH-5430 Wettingen
SWITZERLAND

AEA Technology
Attn: J. H. Rees
D5W/29 Culham Laboratory
Abington, Oxfordshire OX14 3DB
UNITED KINGDOM

AEA Technology
Attn: W. R. Rodwell
044/A31 Winfrith Technical Centre
Dorchester, Dorset DT2 8DH
UNITED KINGDOM

AEA Technology
Attn: J. E. Tinson
B4244 Harwell Laboratory
Didcot, Oxfordshire OX11 ORA
UNITED KINGDOM

Internal

MS	Org.	
0701	6100	L. Shephard
0735	6115	P. B. Davies
0737	6831	E. J. Nowak
0737	6833	J. R. Tillerson
0779	6849	D. R. Anderson
0779	6848	H. N. Jow
0771	6800	M. Chu
0733	6832	J. T. Holmes
1395	6821	M. Marietta
1395	6810	N. Z. Elkins
1395	6860	R. D. Waters
1395	6810	F. D. Hansen
0731	6811	K. Hart (2)
0731	6811	NWM Library (12)
9018	8940-2	Central Technical Files
0899	4916	Technical Library (2)
0619	15102	Review and Approval Desk, For DOE/OSTI